



# Eulerian finite element method for the numerical modeling of fluid dynamics of natural and pathological aortic valves

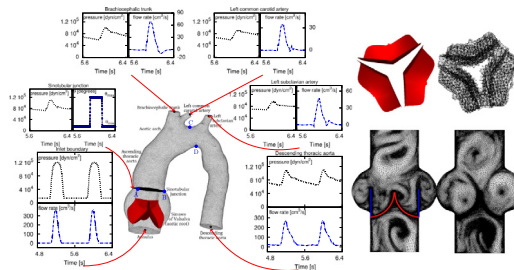
Aymen Laadhari\*, Gábor Székely

<sup>a</sup> Computer Vision Laboratory, Institut für Bildverarbeitung, Department of Information Technology and Electrical Engineering, Swiss Federal Institute of Technology Zürich (Eidgenössische Technische Hochschule Zürich, ETH-Zentrum), CH-8092 Zürich, Switzerland

## HIGHLIGHTS

- Hemodynamics in full aorta and aortic sinuses coupled with highly deformable valve.
- An exact Lagrange multiplier technique couples the dynamics of valve and flow.
- A damped-Newton strategy allows more stability for relatively large Reynolds numbers.
- Numerical examples in 2D and 3D with healthy and pathological valves.
- Numerical investigations pinpoint a risk of blood stagnation after TAVI.

## GRAPHICAL ABSTRACT



## ARTICLE INFO

### Article history:

Received 28 March 2016

Received in revised form 18 October 2016

### MSC:

35Qxx

65Lxx

65Nxx

65Yxx

76-xx

### Keywords:

Computational hemodynamics

Finite element method

Lagrange multiplier

Damped Newton

Aortic valve

Aorta

## ABSTRACT

We present a finite element methodology tailored for the simulation of pulsatile flow in the full aorta and sinus of Valsalva interacting with highly deformable thin leaflets. We describe an extension of the so-called “Resistive Immersed Surface” method. To circumvent stability issues resulting from the bad conditioning of the linear system, especially when flow and geometry become complex after the inclusion of the aorta, we use a Lagrange multiplier technique that couples the dynamics of valve and flow. A banded level set variant allows to address the singularity of the resulting linear system while featuring, in addition to the parallel implementation, higher accuracy and an affordable computational burden. High-fidelity computational geometries are built and simulations are performed under physiological conditions. Several numerical experiments illustrate the ability of the model to capture the basic fluidic phenomena in both healthy and pathological configurations. We finally examine numerically the flow dynamics in the sinus of Valsalva after Transcatheter Aortic Valve Implantation. We show numerically that flow may be subject to stagnation in the lower part of the sinuses. We highlight the far-

\* Corresponding author.

E-mail address: [laadhari@vision.ee.ethz.ch](mailto:laadhari@vision.ee.ethz.ch) (A. Laadhari).

reaching implications of this phenomenon and we hope inciting adequate studies to further investigate its potential clinical consequences.

© 2016 Elsevier B.V. All rights reserved.

## 1. Introduction

The aortic valve, referred to as AV, permits oxygenated blood to circulate from the left ventricle through the systemic circulation. It has three leaflets (or cusps) of very similar size which behave stiff but compliant. They are faced by three corresponding pouches of the aorta called sinus of Valsalva (SV). Leaflets are thin elastic structures ( $\approx 0.2\text{--}0.4$  mm thickness) with complex anatomical features characterized by a non-homogeneous fibrous texture [1]. They synchronize the opening in early systole [2], whereas they are driven to closure in late systole by both the fluid vortices trapped within the sinuses [3, 4] and the deceleration of the aortic flow [5]. Backflow is prevented during diastole in which high transvalvular pressure jump occurs [6]. Valvular pathologies, such as stenosis and regurgitation, can affect the normal functioning of valves leading to the deterioration of life quality. Advancing the computational understanding of the main processes of the valve function, boosted by the recent advances in mathematics and computer science, is certainly of great potential in the development and improvement of novel therapies. In spite of increasing interest in the modeling of valves and blood flow in the full aorta, this coupled problem remains extremely challenging even for commercial software packages. Numerical difficulties include e.g. the resolution of full fluid–structure interaction problem with large and fast deformations of thin structures, substantial mesh deformations, high physiological transvalvular pressure discontinuities, handling contact between cusps when coaptation occurs, stability issues when flow becomes complex or in pathological cases where transition to turbulence may occur.

A variety of methods have been developed to model the valves, while considering different levels of complexity. Zero-dimensional models represent a simplified formalism used to provide computationally cheap physiological description [1,7–9]. Typically, they allow to set the boundary conditions while being unable to capture the full three-dimensional flow pattern near the valve [10–12]. Similarly, the one-dimensional models [13,4] are widely used in multiscale strategies to avoid the three-dimensional modeling of valves [14,15].

Regarding the full three-dimensional modeling of flow in the SV, the coupling of the flow and valve motion is problematic. Numerical approaches remain computationally demanding and several model simplifications are required to tackle this problem. The Arbitrary Lagrangian Eulerian formulation is ruled out since it is limited to small and moderate structural deformations [1,16–19]. Various strategies have investigated the elasticity of the leaflets without capturing the hemodynamics in the surroundings [20]. Concerning the interaction with flow dynamics, several works have used commercial softwares to model thick cusps while modeling the contact between leaflets using penalization approaches [21,22]. The Immersed Boundary Method (IBM) has been used in [13,23–25] and in the pioneering work of Griffith et al. [26,27,25]. The major limitations of such methodologies remain the high computational burden needed for simulations at physiological conditions. Recently a purely fluid model was introduced by Laadhari et al. [28] following [6] where the mechanical properties of the leaflets were disregarded. The model features a relatively simple and straightforward implementation and allows significant computational savings with respect to a full FSI problem, while being able to capture the full three-dimensional description of flow near the valve. First results are shown promising, but the model needs to be further explored and enriched.

Another challenging problem, tightly related to this context, is the modeling of hemodynamics in the sinus of Valsalva after Transcatheter Aortic Valve Implantation, referred to as TAVI. A large number of patients suffering from severe aortic stenosis are not eligible for surgical AV replacement such as elderly (high risk of operative mortality) and younger patients (inoperable until older ages to avoid multiple invasive surgeries). With more than 100.000 implantations performed worldwide [29], TAVI enables the valve replacement without an open-heart surgery and consists in placing a prosthetic valve mounted on a catheter guided stent into a native AV. The heavily calcified native cusps behave usually rigid and play the role of stiff walls fixed by the stent. Cusp stiffness of severe stenosis results from an increase in bone matrix production leading to the endochondral bone tissue formation, where various factors promoting osteogenesis (bone morphogenetic protein-2 and -4) are present [30]. Despite the growing literature devoted to the experimental research in this field, little progress has been reported up to now in the area of computational investigations of hemodynamics after TAVI. Computational studies can advance the understanding of the hemodynamical implication of TAVI. Observing blood stagnation and low velocity areas may represent an evaluating criterion of the TAVI efficiency. Clinically, they are considered as a source for increased probability of thrombosis and embolism (dislodged clot becomes free-floating) which may trigger stroke or heart attack. Note that stagnation is a well-known major life-threatening complication for patients with mechanical AV prosthesis [31]. To the best of our knowledge, there are no similar numerical investigations for blood flow after TAVI.

The aim of the present work is to present a model to study the fluid dynamics in full aorta and SV at reasonable computational burden, whilst being able to capture the three-dimensional flow patterns near the valve. Building on earlier work by Laadhari et al. [28], we improve the existing models to easily perform the full aortic flow simulations. While the original model [6] disregards the opening and closing processes, the model presented in [28] allows to capture the movement of the leaflets but often suffers from instabilities resulting from the setting of the penalty parameter. Indeed, the so-called

“Resistive Immersed Surface” model, referred to as RISM, introduces a penalty term that penalizes the mismatch between the valve and flow velocities. The main drawbacks of such a model is that the valve behaves like a porous media if the penalty parameter is small (unphysiological scenario of leakage across the leaflets), while the conditioning of the linear system becomes deteriorated when the penalty parameter is set too large. Accordingly, the choice of the penalty parameter is problematic and the compromise between large and small values is difficult to properly set especially when the flow and geometry become complex. This problem arises particularly when simulating the hemodynamics in the full aorta and SV.

The present model features the enforcement of the coupling between blood flow and leaflets’ velocities throughout an exact Lagrange multiplier, which addresses several instability issues related to the RISM. The resulting linear system is singular because the constraints are only localized on the leaflets. This issue is addressed by using a banded level set variant, that also enables to significantly reduce the problem size, leading thereby to a similar computational cost to the RISM. Based on the investigation of the performances of various numerical strategies with respect to the flow complexity, we state the global solution method. That ensures further stability when complex flow patterns hold. Moreover, this work enables to model the fluid dynamics in full aorta and SV, while allowing the three-dimensional description of the leaflets which, to our knowledge, represents one of few works, following those of Griffith et al. using the IBM [27]. Our method is entirely based on finite element approximation on unstructured meshes. We employ an anisotropic mesh adaptation technique to improve the computational accuracy in 2D and evaluate at high precision the extent of stagnation zones. We present several numerical experiments showing the robustness and reliability of the model. Quantitative comparisons with respect to clinical measurements and existent numerical results are performed. Finally, to our knowledge, this work presents the first computational study of the hemodynamics in the SV after TAVI. Computational results pinpoint that significant modifications of flow patterns can occur in the lower part of the sinuses, in which flow may be subject to stagnation promoting subsequently a high risk of thromboembolism.

The paper is organized as follows. In Section 2, we provide the mathematical setting for the valve model and the interactions with the fluid dynamics. After studying the sparsity pattern of the global matrix, a banded level set variant is described in Section 3. In Section 4 several numerical experiments are presented under healthy and pathological physiological conditions. We thereafter investigate numerically the incidence of blood stagnation after TAVI. We close with some comments about the findings, model limitations and forthcoming extensions in Section 5.

## 2. Mathematical formulation

In this section, we describe the mathematical setting for the model coupling the dynamics of flow and valve.

### 2.1. Direct formulation of the model

It was pointed out in several studies [32] that blood in the aorta and large vasculature remains laminar, and its viscosity can be assumed constant since the average shear rate is high enough ( $> 150 \text{ s}^{-1}$ ) [33,34]. In healthy humans, a fully developed turbulence is only observed under particular circumstances [32], and the deceleration phase may be not sufficiently long to allow a turbulence regime to develop [35]. However, flow instabilities can occur in the deceleration phase during the systole [36]. The transition to a fully turbulent regime can occur in the case of certain cardiovascular diseases, e.g. severe stenosis, where the narrowing of the cross-sectional area increases the flow instabilities. In this work, we assume blood to be laminar [6,26]. The Navier–Stokes equations represent a reasonable approximation of blood as homogeneous, incompressible and Newtonian fluid.

Let  $T > 0$  represent the period of few cardiac cycles. For any time  $t \in (0, T)$ , let  $\Omega(t) \subset \mathbb{R}^d$ ,  $d = 2, 3$ , denote the domain occupied by the blood and valve, and having a Lipschitz continuous boundary  $\partial\Omega(t)$ . Let  $\mathbf{n}$  be the unit outward normal vector to  $\partial\Omega(t)$ . Let  $\mathbf{u}$  and  $\mathbf{u}^*$  denote the velocities of flow and leaflets, respectively. The set of leaflets is denoted by  $\mathcal{N} = \{1, 2, 3\}$ , while  $\delta_{\Gamma_i}$  with  $i \in \mathcal{N}$  represent the Dirac measure on each leaflet. Since blood follows the movement of the valve, the no-slip condition  $\mathbf{u} - \mathbf{u}_i^* = \mathbf{0}$  on  $(0, T) \times \Gamma_i$ ,  $i \in \mathcal{N}$ , is needed.

As pointed out above, the RISM penalizes the deviation from the latter constraint [28]. However, the method suffers from stability issues if the penalty parameter is set too large, whereas it delivers unphysiological results when choosing small penalty parameters. To properly address this issue, we introduce an exact Lagrange multiplier  $\lambda$  that enables to enforce the matching between the velocities of blood and leaflets on  $\Gamma_i$ ,  $i \in \mathcal{N}$ . This Lagrange multiplier can be physically interpreted as the traction force between the flow and valve. Let  $\boldsymbol{\sigma}(\mathbf{u}, p) = 2\mu\mathbf{D}(\mathbf{u}) - p\mathbf{I}$  be the Cauchy stress tensor, where  $\mathbf{D}(\mathbf{u}) = (\nabla\mathbf{u} + \nabla\mathbf{u}^T)/2$  and  $\mathbf{I}$  represent the strain and identity tensors, respectively. We assume constant density  $\rho$  and dynamic viscosity  $\mu$ . The coupled problem reads:

find the velocity  $\mathbf{u}$ , pressure  $p$  and Lagrange multiplier  $\lambda$  such that

$$\rho \left( \frac{\partial \mathbf{u}}{\partial t} + \mathbf{u} \cdot \nabla \mathbf{u} \right) - \operatorname{div} \boldsymbol{\sigma}(\mathbf{u}, p) + \sum_{i \in \mathcal{N}} \delta_{\Gamma_i} \lambda = \mathbf{0} \quad \text{in } (0, T) \times \Omega, \quad (2.1)$$

$$\operatorname{div} \mathbf{u} = 0 \quad \text{in } (0, T) \times \Omega. \quad (2.2)$$

$$\mathbf{u} - \mathbf{u}_i^* = \mathbf{0} \quad \text{on } (0, T) \times \Gamma_i, \forall i \in \mathcal{N}. \quad (2.3)$$

The interface conditions enforce the continuity of the velocity  $[[\mathbf{u}]] = \mathbf{0}$  across  $\Gamma_{i \in \mathcal{N}}$ , whereas the Lagrange multiplier  $\lambda$  helps to calibrate the discontinuity of the normal stress across  $\Gamma_{i \in \mathcal{N}}$  such that  $[[\boldsymbol{\sigma}\mathbf{n}]] = -\lambda$ . We introduce the Reynolds number  $Re = \rho UD/\mu$  which expresses the ratio between inertial forces and viscous effects based on the maximum instantaneous velocity  $U$  and the diameter  $D$  of the sinotubular junction, see Fig. 18.

Initial conditions are required for the velocity and the leaflets shapes:  $\mathbf{u}(0, \cdot) = \mathbf{u}_0(\cdot)$  and  $\Gamma_i(t = 0) = \Gamma_{i,0}, \forall i \in \mathcal{N}$ . We assume sufficient regularity for the leaflets shapes. Suitable boundary conditions (BCs) ensure the well-posedness of the problem. For given  $\mathbf{u}_b$  and  $\bar{p}$ , let  $\Gamma_D$  and  $\Gamma_N$  represent two complementary subsets of  $\partial\Omega$  on which essential and natural BCs are assigned, respectively. We have  $\mathbf{u} = \mathbf{u}_b$  on  $(0, T) \times \Gamma_D$ , while the natural boundary condition consists in prescribing the normal component of the normal Cauchy stresses:  $\boldsymbol{\sigma}\mathbf{n} = -\bar{p}\mathbf{n}$  on  $(0, T) \times \Gamma_N$ . In Examples 1,  $\Gamma_D = \Gamma_w \cup \Gamma_{in}$  and  $\Gamma_N = \partial\Omega \setminus \Gamma_D$ . In Examples 2-3-4-5,  $\Gamma_D$  is composed of the aortic wall  $\Gamma_w$ , while  $\Gamma_N$  includes the remaining boundaries, see Figs. 3 and 18. In the current work, the aortic wall is assumed rigid following [27], on which we prescribe a homogeneous Dirichlet boundary condition  $\mathbf{u}_b = \mathbf{0}$  on  $\Gamma_w$ .

We consider two ways to set the inlet BC which consist in either prescribing a periodic time-dependent velocity profile (essential BC) or pressure waveform within the physiological range (natural BC). Physiological pressure pulses are always used to set boundary conditions on outlets. A lumped-parameter model, consisting of a three-element Windkessel, allows to estimate the global arterial properties downstream. It consists in an electrical analog with a proximal resistance  $R_p$  placed in series with a total arterial compliance  $C$  and a vascular resistance  $R_d$ , see Fig. 1. Physiological pressures on outlets are obtained by assessing the model parameters in a suitable manner. By performing an electrical analogy, the model results in a second-order ordinary differential equation that describes the relation between the time-dependent pressure  $\bar{p}$  and the volumetric flow rate  $Q$  at the corresponding boundary. The problem reads:

$$\mathcal{P}_{W3E} : \bar{p}(t) + CR_d \frac{d\bar{p}(t)}{dt} = (R_p + R_d) Q(t) + CR_p R_d \frac{dQ(t)}{dt}, \quad t \in (0, T). \tag{2.4}$$

In what follows, we denote  $\Gamma_N = \cup_{k \in K} \Gamma_{N,k}$  where  $K$  represents the set of boundaries on which natural boundary conditions are assigned. The corresponding pressures are called  $\bar{p}_k$  with  $k \in K$ .

To write the variational formulation, we first introduce the spaces of admissible velocities and pressures:

$$\mathbb{V}(\mathbf{u}_b) = \left\{ \mathbf{v} \in (H^1(\Omega))^d : \mathbf{v} = \mathbf{u}_b \text{ on } \Sigma_D \right\} \quad \text{and} \quad \mathbb{Q} = \left\{ q \in L^2(\Omega) : \int_{\Omega} q \, dx = 0 \right\}.$$

Testing ((2.1)–(2.2)–(2.3)) against suitable functions, the problem reads:

$\mathcal{P}_0$ : find  $\mathbf{u} \in \mathcal{C}^0((0, T), L^2(\Omega)^d) \cap L^2((0, T), \mathbb{V}(\mathbf{u}_b))$ ,  $p \in L^2((0, T), \mathbb{Q})$  and  $\lambda \in L^2((0, T), H^{-\frac{1}{2}}(\cup_{i \in \mathcal{N}} \Gamma_i)^d)$  such that

$$\int_{\Omega} \rho \left( \frac{\partial \mathbf{u}}{\partial t} + \mathbf{u} \cdot \nabla \mathbf{u} \right) \cdot \mathbf{v} + \int_{\Omega} 2\mu \mathbf{D}(\mathbf{u}) : \mathbf{D}(\mathbf{v}) - \int_{\Omega} p \operatorname{div} \mathbf{v} + \sum_{i \in \mathcal{N}} \int_{\Gamma_i} \lambda \cdot \mathbf{v} = \sum_{k \in K} \int_{\Gamma_{N,k}} \bar{p}_k \mathbf{n} \cdot \mathbf{v}, \quad \forall \mathbf{v} \in \mathbb{V}(0), \tag{2.5a}$$

$$\int_{\Omega} q \operatorname{div} \mathbf{u} = 0, \quad \forall q \in L^2(\Omega), \tag{2.5b}$$

$$\sum_{i \in \mathcal{N}} \int_{\Gamma_i} \boldsymbol{\xi} \cdot (\mathbf{u} - \mathbf{u}_i^*) = 0, \quad \forall \boldsymbol{\xi} \in H^{-\frac{1}{2}}(\cup_{i \in \mathcal{N}} \Gamma_i)^d. \tag{2.5c}$$

Let us consider some quantities of clinical relevance. Let  $\otimes$  denote the tensorial product between vectors and  $T^*$  be the cardiac cycle period. We introduce the wall shear stress **WSS**, the time-averaged wall shear stress AWSSV, the time-averaged wall shear stress magnitude AWSSM and the oscillatory shear index OSI as follows:

$$\frac{\mathbf{WSS}}{2\mu} = (\mathbf{I} - \mathbf{n} \otimes \mathbf{n}) \mathbf{D}(\mathbf{u})\mathbf{n}, \quad \text{AWSSV} = \left| \int_0^{T^*} \frac{\mathbf{WSS}}{T^*} \right|, \quad \text{AWSSM} = \frac{1}{T^*} \int_0^{T^*} |\mathbf{WSS}| \quad \text{and}$$

$$\text{OSI} = \frac{1}{2} \left( 1 - \frac{\text{AWSSV}}{\text{AWSSM}} \right).$$

The WSS is frequently employed by medical doctors in diagnosis and clinical decision-making. It represents the tangential drag force per unit area induced by the tangential movement of blood and experienced by the aortic wall. It is given by the tangential component of the normal stress tensor. The AWSSV represents the time-averaged shear stress that the arterial wall is subjected to over the cardiac cycle. The OSI indicates the deflection of the WSS from the flow predominant direction along the cardiac cycle. It varies from 0 when no cyclic directional changes are observed to 0.5 obtained when  $2\pi$  radian deflection of the WSS vector is observed.

To compute the WSS, let  $\nabla_{\parallel} \equiv (\mathbf{I} - \mathbf{n} \otimes \mathbf{n}) \nabla$  be the two-dimensional gradient operator evaluated in the tangent plane to  $\Gamma_w$ . In the local coordinate system,  $\mathbf{u}$  expresses  $(\hat{u}_1, \hat{u}_2, \hat{u}_3)^T$ . Because of the rigidity assumption of the aortic wall, the relation  $\nabla_{\parallel} \hat{u}_3 = \mathbf{0}$  holds. By writing **WSS** in the local frame of reference, a straightforward simpler relation is obtained:  $\mathbf{WSS} = \mu (\hat{w}_2, -\hat{w}_1, 0)^T$  where  $\mathbf{w} \equiv (\hat{w}_1, \hat{w}_2, \hat{w}_3)^T = \operatorname{curl} \mathbf{u}$ . Consequently, we obtain  $|\mathbf{WSS}| = \mu |\operatorname{curl} \mathbf{u}|$ .

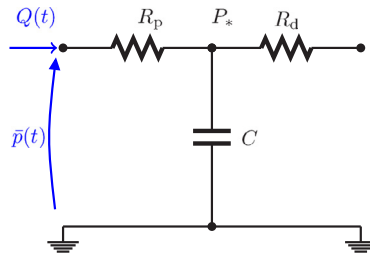


Fig. 1. Schematic representation of the three-element Windkessel model used to prescribe physiological pressure waveform on outlets.

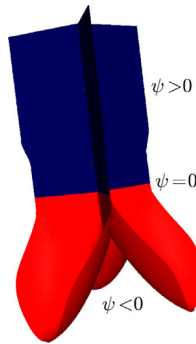


Fig. 2. Illustration of the Eulerian representation of the tricuspid aortic valve.

## 2.2. Valve model

### 2.2.1. Eulerian description of leaflets

The geometrical description of the leaflets can be typically performed using either boundary-conforming (Lagrangian) or non-boundary conforming (Eulerian) approaches. In a Lagrangian framework, a mesh fitting the leaflets follows explicitly their movement. A robust remeshing tool is required to remesh the computational domain, while avoiding the generation of reversed elements. In an Eulerian framework, the leaflets are implicitly described and the remeshing is not required. Each leaflet is geometrically considered as an open surface, which is defined as a co-dimension one of a manifold having a boundary (free edge and intersection with the aortic wall) and embedded in the three-dimensional Euclidean space. Accordingly, we use a construction based on two level set embedding functions [28]. Each leaflet  $\Gamma_i, i \in \mathcal{N}$  is described using a primary level set  $\varphi_i$  and a secondary level set  $\psi_i$  such that:

$$\Gamma_i(t) = \left\{ \mathbf{x}(t) \in \Omega : \varphi_i(t; \mathbf{x}) = 0 \text{ and } \psi_i(t; \mathbf{x}) \leq 0 \right\}, \quad t \in (0, T), \quad i \in \mathcal{N}. \tag{2.6}$$

The function  $\psi$  enables to circumscribe the area where the zero-level set of  $\varphi$  describes the leaflet as illustrated in Fig. 2. We use second-order algebraic descriptions for the leaflets at both open and closed positions. The corresponding real coefficients are obtained by fixing some descriptors introduced to build a high-fidelity computational geometry of the leaflets based on some experimental measurements available in the published literature [37–40]. To avoid having too large or too small gradients in the vicinity of the leaflets, we proceed with a preprocessing step that enables to redress the level set functions  $\varphi_i, i \in \mathcal{N}$ , as signed distance functions. We disregard the mechanical properties of the leaflets, whereas we focus on investigating the capability of this model to study the fluid dynamics in the full aorta while considering the three-dimensional valvular shapes.

The problem  $\mathcal{P}_0$  involves integrals over the moving leaflets  $\Gamma_i, i \in \mathcal{N}$ . In a purely Lagrangian framework, these integrals need a mesh that explicitly fits the leaflets. To avoid tackling remeshing issues resulting from the large deformations and quick movement of the leaflets, all surface integrals are replaced by their regularized counterparts, see e.g. [41]. Let  $\varepsilon$  be a regularization parameter proportional to the local mesh size. The sharp Heaviside function  $\mathcal{H}$  and Dirac measure  $\delta$  are regularized within a banded region of width  $2\varepsilon$  as follows:

$$\mathcal{H}_\varepsilon(\phi) = \begin{cases} 0, & \text{if } \phi < -\varepsilon \\ \frac{1}{2} \left( 1 + \frac{\phi}{\varepsilon} + \frac{\sin\left(\frac{\pi\phi}{\varepsilon}\right)}{\pi} \right), & \text{if } |\phi| \leq \varepsilon \\ 1 & \text{otherwise.} \end{cases} \quad \text{and} \quad \delta_\varepsilon(\phi) = \begin{cases} \frac{1}{2\varepsilon} \left( 1 + \cos\left(\frac{\pi\phi}{\varepsilon}\right) \right), & \text{if } |\phi| \leq \varepsilon \\ 0 & \text{otherwise.} \end{cases}$$

Hence, the surface integrals in  $\mathcal{P}_0$  are replaced by integrals over the entire domain  $\Omega$ , leading to a regularized problem  $\mathcal{P}_\varepsilon(\mathbf{u}; p, \lambda)$ . In particular, we have:

$$\sum_{i \in \mathcal{N}} \int_{\Gamma_i} \lambda \cdot \mathbf{v} \, ds \approx \int_{\Omega} \sum_{i \in \mathcal{N}} |\nabla \varphi_i| \delta_\varepsilon(\varphi_i) \mathcal{H}_\varepsilon(1 - \psi_i) \lambda \cdot \mathbf{v} \, d\mathbf{x}.$$

We now focus on the computation of the leaflets' velocities  $\mathbf{u}_i^*$  with  $i \in \mathcal{N}$ . Since every material point  $\mathbf{x}(t) \in \Gamma_i(t)$  shall verify the equation  $\varphi_i(t, \mathbf{x}(t)) = 0$ , the time derivative leads to  $\partial_t \varphi_i + \mathbf{u}_i^* \cdot \nabla \varphi_i = 0$  with  $\mathbf{u}_i^* \equiv \partial_t \mathbf{x}$  on  $\Gamma_i$ . Since  $\nabla \varphi_i$  describes the normal direction to  $\Gamma_i$ ,  $i \in \mathcal{N}$ , only the normal component of the cusp's velocity has an effective contribution to its motion. Let  $\Delta t$  be the time step size and  $\varphi_i^n$  be the computed solution at time  $t^n$ . By considering a second order differentiation formula, the velocity of the leaflet  $\Gamma_i$  can be approximated by:

$$\mathbf{u}_i^*(t^n) \approx \frac{-3\varphi_i^n + 4\varphi_i^{n-1} - \varphi_i^{n-2}}{2\Delta t} \frac{\nabla \varphi_i^n}{|\nabla \varphi_i^n|^2}, \quad \forall i \in \mathcal{N}.$$

In the case of TAVI, we assume that the native leaflets, referred to as  $S_i$  with  $i \in \mathcal{N}$ , are highly calcified and behave stiff. Accordingly, we assume  $\mathbf{u}_{S_i}^* = \mathbf{0}$  for all  $i \in \mathcal{N}$ .

### 2.2.2. Reduced order model for the dynamics of valves

We aim to couple the three-dimensional model describing the fluid dynamics with a reduced-order model tracking the movement of anatomically correct three-dimensional valve. Although the reduced-order models are less detailed than three-dimensional distributed parameter models, they enable to circumvent several numerical difficulties related to the large displacements of the leaflets, whilst capturing the three-dimensional flow profile around the valve. To achieve this purpose, a geometrical multiscale coupling model enables to follow the cusps movement described through their aperture angle  $\theta$ . Based on experimental and clinical observations, Korakianitis and Shi introduced a reduced order model describing the valve movement as a function of  $\theta$  [8]. Indeed, the dynamics is analyzed by considering the hemodynamical characterization of the flow upstream and downstream the valve during the cardiac cycle. The model balances the angular cusp acceleration with various angular momenta affecting the valve motion due to the friction from neighboring tissue resistance, the transvalvular pressure gradient  $\Delta P$ , the dynamic motion of blood acting on the cusps, and the effect of downstream vortices. The model reads:

$$\mathcal{P}_\theta : \frac{d^2\theta}{dt^2} + \Psi_f \frac{d\theta}{dt} = \Psi_p \Delta P \cos \theta + \Psi_q Q \cos \theta + \Psi_v Q \sin 2\theta \frac{\max(\Delta P, 0)}{\Delta P}, \quad \theta \in [\theta_{\min}, \theta_{\max}]$$

with  $\Psi_f = 50 \text{ s}^{-1}$ ,  $\Psi_p = 4.125 \frac{\text{rad cm}^2}{\text{s}^2 \text{ dyn}}$ ,  $\Psi_q = 2 \frac{\text{rad}}{\text{s cm}^3}$  and  $\Psi_v = 7 \frac{\text{rad}}{\text{s cm}^3}$ .

At the numerical level, we approximate the left ventricular and the aortic pressures by the mean pressures measured on the annulus proximal to the valve and the sinotubular junction, respectively, as depicted in Fig. 18.

This model was validated, as it provided comparable numerical results to those illustrated in medical textbooks, see [8]. The non-binary valve state is then described through a state parameter:  $\mathcal{E}(\theta) = (\cos \theta_{\min} - \cos \theta)^2 / (\cos \theta_{\min} - \cos \theta_{\max})^2$ . The minimal angle  $\theta_{\min}$  corresponds to a fully closed position, i.e.  $\mathcal{E} = 0$ , whereas the maximum opening angle  $\theta_{\max}$  corresponds to a fully open position, i.e.  $\mathcal{E} = 1$ . The state parameter  $\mathcal{E} \in [0, 1]$  enables to determine the leaflets geometrical shape  $\Gamma_i(t)$ ,  $i \in \mathcal{N}$ , at any intermediate position by interpolating the functions  $\varphi_i$  and  $\psi_i$  describing the valve at the fully open and fully closed positions.

This model enables to readily recover different pathological scenarios including regurgitation and stenosis. Stenosis is modeled by restricting the maximum opening angle  $\theta_{\max}$ , while it suffices to constraint the minimal angle  $\theta_{\min}$  in the regurgitant case by imposing a larger value that prevents the valve to completely close. In the examples,  $\theta \in [5, 75]^\circ$  in the healthy case, while  $\theta_{\max} = 59^\circ$  in the stenotic case. To improve the accuracy during the prompt opening and closing processes, we reduce the time step size during these events. A boolean function `valveState` is considered and returns the Boolean value `false` whenever the left ventricular pressure exceeds the aortic pressure for a closed valve, or when a backflow is observed for a fully open valve, see the graphical illustration in Fig. 10.

### 3. Numerical approximation and implementation details

In this section we first recapitulate the computational geometries and the meshing tools/procedures used in both 2D and 3D. The method used to approximate the Windkessel model is then briefly presented. We subsequently discuss the sparsity pattern of the global matrix and we state the assembling approach. Finally, we describe the solution method based on the results of different algorithmic choices and the parallel performances.

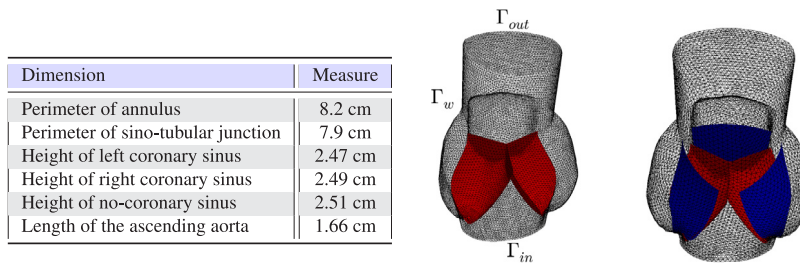


**Fig. 3.** Left: Dimensions and nomenclature of the sinus of Valsalva in the three-dimensional case. Middle: FE network for a healthy valve. Right: TAVI with healthy (red) and calcified (blue) leaflets. (For interpretation of the references to color in this figure legend, the reader is referred to the web version of this article.)

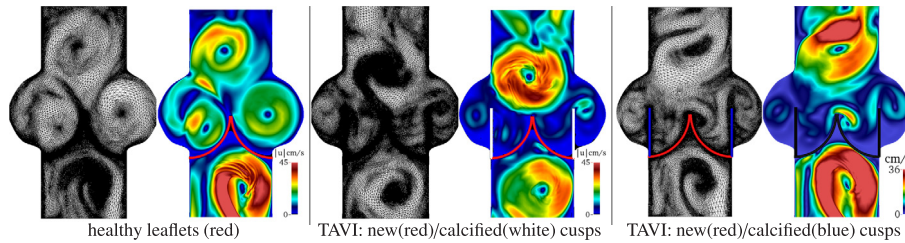


**Fig. 4.** Set-up and mesh adaptation in the two-dimensional case. Adapted meshes and corresponding velocity solution in both cases of healthy aortic valve and TAVI.

### 3.1. Handling of geometries and meshes

*Realistic computational geometries in 3D.* Three computational geometries are considered in our 3D examples. First, the geometry of the aortic root in Example (4.1.1), Example (4.3) and Example (4.5) is made up of the left ventricular outflow tract, the SV, the sino-tubular junction and a portion of the ascending aorta, see Fig. 3. Although the geometry is not patient-specific, various anatomical dimensions are respected and we base the geometry construction on the data reported in [37–40]. The computational domain and the characteristic dimensions are reported in Fig. 3.

Second, the geometry of the aorta used in Example (4.4) is patient-specific and obtained from MRI images. The original mesh can be found on the Gmsh website.<sup>1</sup> The mesh depicted in Fig. 18 is built by joining the aorta on the top of the aforementioned geometry of the aortic root. To that end, the initial surface mesh in the stereolithography (STL) format is repaired and locally smoothed by using the softwares MeshLab<sup>2</sup> and Netfabb.<sup>3</sup> This triangular mesh is then remeshed using the Frontal algorithm in Gmsh. Volumetric meshes, composed by fully unstructured tetrahedral elements, are subsequently constructed using Gmsh. We also use the open-source optimizer from Netgen [42] to enhance the tetrahedral mesh quality by maximizing the ratio between the radii of the inscribed and the circumscribed spheres in each tetrahedra. We thereafter use the software Autodesk Maya<sup>4</sup> to properly combine the aorta and the aortic root at the level of the sinotubular junction.

Finally, the patient-specific geometry used in Example (4.1.2) belongs to a 17-year old subject with a mild thoracic aortic coarctation. The tetrahedral mesh is obtained by first attaching the geometry of the SV to the patient-specific aorta, and then meshing the entire geometry by following the aforementioned procedure.

*Geometries in 2D and mesh adaptation technique.* In the two-dimensional case, we use the same geometry designed in [43], see Fig. 4. Although the flow through the AV is inherently 3D, the legitimacy of a 2D geometry is supported by the good agreement between the numerical results of hemodynamics in 2D, the in vitro ultrasound measurements and the ex vivo studies revealed in [43]. We also use an adaptive mesh refinement procedure that particularly helps to accurately capture the stagnation and the recirculation zones with high mesh density therein. Moreover, it enables to enhance the computational accuracy in areas with complex flow patterns, see Fig. 4.

The technique is based on the work of [44], and we use the bidirectional anisotropic mesh generator BAMG [45]. Based on the computation of the metric tensor of a given criterion  $\zeta$ , the mesh is adapted in such a way that the interpolation error becomes equidistributed, and the maximal and minimal directions of stretching become adjusted to the directions of maximal and minimal errors. We refer to [41] for a detailed description of the meshing procedure. In the present work, we

<sup>1</sup> Gmsh—<http://www.geuz.org/gmsh>.

<sup>2</sup> MeshLab—<http://meshlab.sourceforge.net>.

<sup>3</sup> Netfabb—<http://www.netfabb.com>.

<sup>4</sup> Maya—<http://www.autodesk.com/products/maya>.

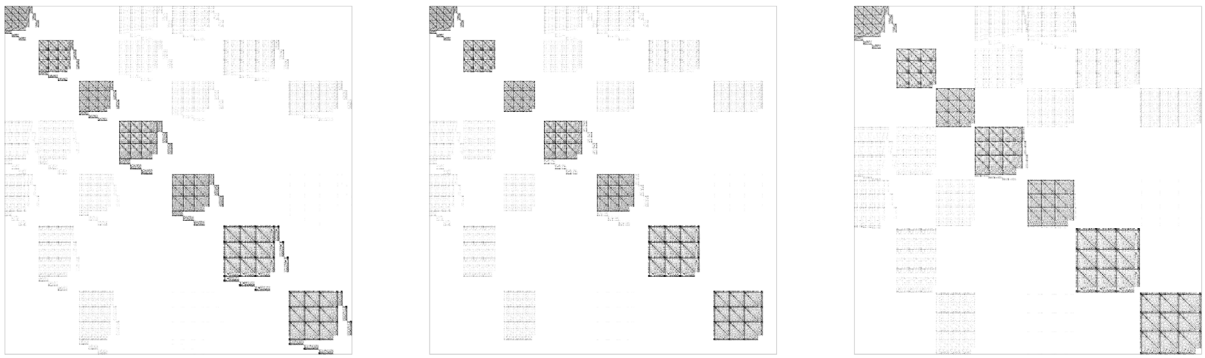


**Fig. 5.** Sparsity pattern of the global matrix exported in the standard Matrix-Market format. Left: Constraint (2.3) extended to the entire  $\Omega$  (matrix size =  $7313^2$ ). Middle: Discretized problem  $\mathcal{P}_\varepsilon$  with  $\lambda \in \Omega$  (matrix size =  $7313^2$ ). Right: Discretized problem  $\mathcal{P}_\varepsilon$  with  $\lambda_h \in B_{h,\varepsilon}$  (matrix size =  $5855^2$ ). The size of the global matrix obtained using the Resistive Immersed Surface method is equal to  $5534^2$ .

introduce a different meshing criterion aggregating the kinetic and viscous energies at every time step. The corresponding Hessian matrix reads:

$$\mathbf{H} \equiv \nabla \nabla_{\mathcal{S}}(\mathbf{u}_h) = \nabla \nabla \left( \frac{\rho}{2} |\mathbf{u}_h|^2 + 2\mu |\mathbf{D}(\mathbf{u}_h)|^2 \right)^{1/2}.$$

We use an  $L^2$  projection to obtain a piecewise linear and continuous approximation of the metric matrix. Some generated meshes and the corresponding velocity solution in both cases of healthy AV and TAVI are depicted in Fig. 4. We clearly see the various meshes highly refined according to the flow vortices and also in the vicinity of the healthy and calcified leaflets. More accurate computations are then expected, in particular when quantifying the stagnation zones in Example (4.5), see Movie 1 in the supplementary material (see Appendix A). The extension of this approach to the three-dimensional case remains a challenging topic and is definitely beyond the scope of this work.

### 3.2. Sparsity pattern and banded level set approach

We consider a partition  $\mathcal{T}$  of  $\Omega$  consisting of geometrically conforming open simplicial elements  $K$  (triangles for  $d = 2$  or tetrahedra for  $d = 3$ ), such that  $\bar{\Omega} = \cup_{K \in \mathcal{T}} K$ . For all  $K \in \mathcal{T}$ , let  $h_K$  denote the diameter of  $K$ . The mesh size is defined as the largest element diameter  $h = \max_{K \in \mathcal{T}_h} h_K$ . We use the notation  $\mathcal{T}_h$  for a mesh  $\mathcal{T}$  having a mesh size  $h$ .

We intend to give better insight into the structure of the matrix of the linear system corresponding to the discretized problem  $\mathcal{P}_\varepsilon$ . To display the sparsity pattern of the global matrix, we use the particular Matrix-Market format<sup>5</sup> (ASCII-based), and the file is converted afterwards into the Matlab sparse format.<sup>6</sup> The latter format is elaborated in such a way that only the non-zero entries are encoded, and the corresponding coordinates are explicitly stored.

We assemble and visualize the matrix of the linear system of the discretized problem in Fig. 5 (middle), showing a sparse and symmetric block-structure. In addition, this matrix is singular since several rows and columns are empty, and a direct solver cannot be used. Indeed, the Lagrange multiplier  $\lambda$  is required to enforce the constraint (2.3) only in a small surrounding of  $\Gamma_i$ ,  $i \in \mathcal{N}$ , but it was extended to the entire domain  $\Omega$ , see Section 2.2.1. Consequently, zero entries correspond in the global matrix of the linear system to the extended values of  $\lambda$  outside the regularized surfaces  $\Gamma_i$ ,  $i \in \mathcal{N}$ . Hence, the global matrix is not invertible and results in the singularity of the linear system.

To visualize this singularity, we replace the constraint (2.3) by  $\mathbf{u} = \mathbf{u}^*$  in the entire  $\Omega$  (unphysiological meaning), and we assemble the corresponding linear system. In Fig. 5 (left), we observe a block-structured matrix but without the set of empty rows and columns. To address the singularity issue, we rather define the Lagrange multiplier  $\lambda$  only in a banded domain of width  $2\varepsilon$  around the leaflets:

$$B_{h,\varepsilon}(t) = \left\{ K \in \mathcal{T}_h : \delta_\varepsilon(\varphi_i) \neq 0, \forall i \in \mathcal{N} \right\}.$$

Only the coefficients that correspond to these elements are considered in the global matrix. The resulting global matrix is visualized in Fig. 5 (right), showing that the singularity of the global matrix is addressed (empty rows and columns eliminated). Remark that the new linear system has a similar size as the linear system obtained by the RIS method. In summary, the present approach features as similar computational cost as the RIS method and allows to avoid the arbitrary setting of large penalty coefficients that can harm the conditioning of the linear system.

<sup>5</sup> Matrix-Market format—<http://math.nist.gov/MatrixMarket/index.html>.

<sup>6</sup> Matlab—<http://ch.mathworks.com/>.

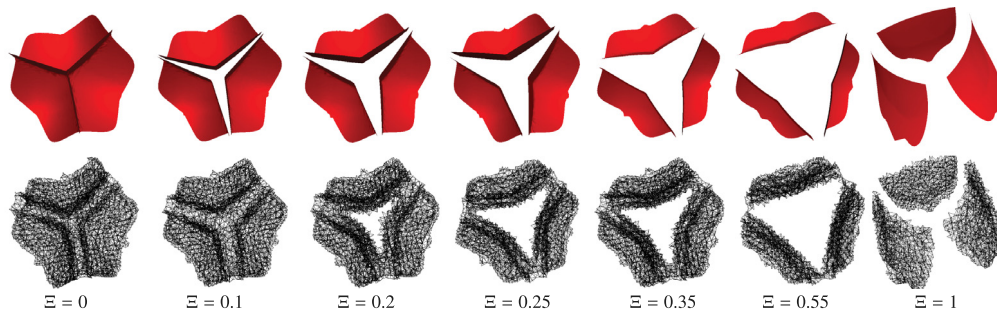


Fig. 6. Snapshots showing the aortic valve and corresponding mesh bands  $B_{h,\epsilon}$  with respect to the state parameter  $\Xi$ .

We introduce the following finite-dimensional spaces:

$$\mathbb{X}_h = \left\{ \mathbf{u} \in (C^0(\overline{\Omega}))^d : \mathbf{u}|_K \in (\mathbb{P}_2(K))^d, \forall K \in \mathcal{T}_h \right\}, \quad \mathbb{V}_h(\mathbf{u}_b) = \mathbb{X}_h \cap \mathbb{V}(\mathbf{u}_b)$$

and

$$\mathbb{Q}_h = \left\{ q \in \mathbb{Q} \cap C^0(\overline{\Omega}) : q|_K \in \mathbb{P}_1(K), \forall K \in \mathcal{T}_h \right\}.$$

To fulfill the inf-sup condition, the Taylor–Hood finite elements are considered for the approximation of the velocity and the pressure [46]. The discretized Lagrange multiplier  $\lambda_h$  belongs to the finite element space:

$$\mathbb{W}_{h,\epsilon} = \left\{ \xi \in (L^2(B_{h,\epsilon}))^d \cap (C^0(X_{h,\epsilon}))^d : \xi|_K \in (\mathbb{P}_2)^d, \forall K \in B_{h,\epsilon} \right\},$$

which depends now on the dynamic movement of the valve. In Fig. 6, we provide snapshots of the mesh bands  $B_{h,\epsilon}$  and the corresponding state parameter  $\Xi$  obtained in the case of a healthy aortic valve.

### 3.3. Fully discrete finite element approximation

In this subsection, we consider a fully discrete variant of the problem  $\mathcal{P}_\epsilon$ . We first present the different implicit strategies, and we set afterwards the solution method with respect to the flow complexity.

We consider the partitioning  $t^n, n = 0, \dots, N - 1$  of  $[0, T]$  into uniform time steps  $\Delta t$ . To follow the fast movement of the leaflets, we proceed with a time step size adaptation (reduction by a factor ten) whenever the valve moves. That enables to better capture the flow pattern during the opening and closing phases. Since the Reynolds number becomes relatively large around the peak of systole (especially in pathological cases), numerical instabilities can be triggered and we similarly proceed with time step reduction when  $Re$  becomes bigger than a fixed threshold value.

For any  $n \geq 1$  and  $i \in \mathcal{N}$ , we denote by  $\mathbf{u}_{\epsilon,h}^n, p_{\epsilon,h}^n, \lambda_{\epsilon,h}^n, \varphi_{i,\epsilon,h}^n$  and  $\psi_{i,\epsilon,h}^n$  the approximation of  $\mathbf{u}_\epsilon, p_\epsilon, \lambda_\epsilon, \varphi_{i,\epsilon}$  and  $\psi_{i,\epsilon}$  in space at time step  $n$ , respectively. For given  $\mathbf{u}, \mathbf{v}, \mathbf{w} \in (H^1(\Omega))^d, p \in L^2(\Omega), w \in L^\infty(\Omega), \mathbf{n} \in (L^\infty(\Gamma_{out,k}))^d$  and  $\bar{p} \in \mathbb{R}$ , we introduce the weighted multi-linear forms:

$$m(\mathbf{u}, \mathbf{v}; w) = \int_{\Omega} w \mathbf{u} \cdot \mathbf{v}; \quad m_{\Gamma_k}(\bar{p}, \mathbf{v}; \mathbf{n}) = \int_{\Gamma_{out,k}} \bar{p} \mathbf{n} \cdot \mathbf{v}; \quad a(\mathbf{u}, \mathbf{v}; w) = \int_{\Omega} 2 w \mathbf{D}(\mathbf{u}) : \mathbf{D}(\mathbf{v});$$

$$b(\mathbf{v}, p) = - \int_{\Omega} p \operatorname{div} \mathbf{v} \quad \text{and} \quad c(\mathbf{u}, \mathbf{v}; w, \mathbf{w}) = \int_{\Lambda} w \left( (\mathbf{u} \cdot \nabla) \mathbf{w} + (\mathbf{w} \cdot \nabla) \mathbf{u} \right) \cdot \mathbf{v}.$$

#### 3.3.1. Strategy I: fixed-point scheme

The nonlinear problem  $\mathcal{P}_\epsilon$  is reduced to a sequence of linear subproblems by using the fixed-point algorithm. We employ a second order characteristics method to approximate the inertia term in (2.1). Let  $\chi(\cdot, \mathbf{x}, t)$  be the characteristic curve passing at time  $t$  through  $\mathbf{x} \in \Omega$ . The material derivative is approximated by

$$\frac{\partial}{\partial \tau} \left( \mathbf{u}(\chi(t^n, \mathbf{x}; \tau), \tau) \right) \Big|_{\tau=t^n} \approx \frac{3\mathbf{u}(t^n, \mathbf{x}) - 4\mathbf{u}(t^{n-1}, \chi_{n-1}^{(1)}(\mathbf{x})) + \mathbf{u}(t^{n-2}, \chi_{n-2}^{(2)}(\mathbf{x}))}{2\Delta t},$$

where  $\tilde{\mathbf{u}} = 2\mathbf{u}^n - \mathbf{u}^{n-1}$  is the second order extrapolation of the velocity,  $\chi_{n-1}^{(1)}(\mathbf{x}) = \mathbf{x} - \Delta t \tilde{\mathbf{u}}(\mathbf{x})$  is the first-order characteristics, and  $\chi_{n-2}^{(2)}(\mathbf{x}) = \mathbf{x} - 2\Delta t \tilde{\mathbf{u}}(\mathbf{x})$  is the second-order characteristics. The overall scheme is detailed in Algorithm 1, where the inner loop is preceded by the computation of the new valve position by solving  $\mathcal{P}_\theta$ . At the computational level, the fixed-point iteration is repeated until the relative error becomes smaller than a given tolerance  $\epsilon_{fp} = 10^{-6}$ . Remark that the fixed-point algorithm might benefit from an adaptive relaxation parameter such as the generalized Aitken method [47].

Since the convergence of the latter method is not always guaranteed, we here restrict ourselves to the fixed-point algorithm and rather focus on Newton-like algorithms.

**Algorithm 1** Fixed-point strategy

- 1: Let  $n = 0$  and  $(\mathbf{u}_{\varepsilon,h}^0, p_{\varepsilon,h}^0, \lambda_{\varepsilon,h}^0)$  be the known initial condition
- 2: **for**  $n = 1, \dots, n_{\max} = T/\Delta t$  **do**
- 3: Let  $(\mathbf{u}_{\varepsilon,h}^{n+1,-1}, p_{\varepsilon,h}^{n+1,-1}, \lambda_{\varepsilon,h}^{n+1,-1}) = (\mathbf{u}_{\varepsilon,h}^{n+1,0}, p_{\varepsilon,h}^{n+1,0}, \lambda_{\varepsilon,h}^{n+1,0}) = (\mathbf{u}_{\varepsilon,h}^n, p_{\varepsilon,h}^n, \lambda_{\varepsilon,h}^n)$  being known
- 4: Compute  $(\varphi_{i,h}^n, \psi_{i,h}^n) \in \mathbb{Q}_h^2, \forall i \in \mathcal{N}$  and  $\mathbf{u}_h^{*,n} \in \mathbb{V}_h(\mathbf{u}_b)$
- 5: **for**  $k = 0, \dots, k_{\max}$  **do**
- 6: Let  $(\mathbf{u}_{\varepsilon,h}^{n+1,k}, p_{\varepsilon,h}^{n+1,k}, \lambda_{\varepsilon,h}^{n+1,k})$  and  $(\mathbf{u}_{\varepsilon,h}^{n+1,k-1}, p_{\varepsilon,h}^{n+1,k-1}, \lambda_{\varepsilon,h}^{n+1,k-1})$  being known
- 7: Solve the following linear subproblem:  
 $\mathcal{P}_{\varepsilon,h}^{n,k}: \text{ find } \mathbf{u}_{\varepsilon,h}^{n+1,k+1} \in \mathbb{V}_h(\mathbf{u}_b), p_{\varepsilon,h}^{n+1,k+1} \in \mathbb{Q}_h \text{ and } \lambda_{\varepsilon,h}^{n+1,k+1} \in \mathbb{W}_h \text{ such that}$   

$$m\left(3\mathbf{u}_{\varepsilon,h}^{n+1,k+1}, \mathbf{v}; \frac{\rho}{2\Delta t}\right) + a\left(\mathbf{u}_{\varepsilon,h}^{n+1,k+1}, \mathbf{v}; \mu\right) + b\left(\mathbf{v}, p_{\varepsilon,h}^{n+1,k+1}\right) + \sum_{i \in \mathcal{N}} m\left(\lambda^{n+1,k+1}, \mathbf{v}; |\nabla \varphi_{i,h}^n| \delta_\varepsilon(\varphi_{i,h}^n) (1 - \mathcal{H}_\varepsilon(\psi_{i,h}^n))\right)$$

$$= m\left(4\mathbf{u}_{\varepsilon,h}^{n+1,k} \circ \chi^{n+1,k} - \mathbf{u}_{\varepsilon,h}^{n+1,k-1} \circ \chi^{n+1,k-1}, \mathbf{v}; \frac{\rho}{2\Delta t}\right) + \sum_{k \in K} m_{\Gamma_k}(\bar{p}_k, \mathbf{v}; \mathbf{n})$$

$$b\left(\mathbf{u}_{\varepsilon,h}^{n+1,k+1}, q\right) = 0$$

$$\sum_{i \in \mathcal{N}} m\left(\mathbf{u}_{\varepsilon,h}^{n+1,k+1}, \mathbf{w}; |\nabla \phi_{i,h}^n| \delta_\varepsilon(\phi_{i,h}^n) (1 - \mathcal{H}_\varepsilon(\psi_{i,h}^n))\right) = \sum_{i \in \mathcal{N}} m\left(\mathbf{u}_h^{*,n}, \mathbf{w}; |\nabla \phi_{i,h}^n| \delta_\varepsilon(\phi_{i,h}^n) (1 - \mathcal{H}_\varepsilon(\psi_{i,h}^n))\right)$$
- 8: **if**  $\frac{|\mathbf{u}_{\varepsilon,h}^{n+1,k+1} - \mathbf{u}_{\varepsilon,h}^{n+1,k}|_{1,\Omega}}{|\mathbf{u}_{\varepsilon,h}^{n+1,k}|_{1,\Omega}} + \frac{|p_{\varepsilon,h}^{n+1,k+1} - p_{\varepsilon,h}^{n+1,k}|_{0,\Omega}}{|p_{\varepsilon,h}^{n+1,k}|_{0,\Omega}} + \sum_{i \in \mathcal{N}} \frac{|\lambda_{\varepsilon,h}^{n+1,k+1} - \lambda_{\varepsilon,h}^{n+1,k}|_{0,\Gamma_i}}{|\lambda_{\varepsilon,h}^{n+1,k}|_{0,\Gamma_i}} \leq \epsilon_{\text{fp}}$  **then**
- 9: Set  $(\mathbf{u}_{\varepsilon,h}^{n+1}, p_{\varepsilon,h}^{n+1}, \lambda_{\varepsilon,h}^{n+1}) = (\mathbf{u}_{\varepsilon,h}^{n+1,k+1}, p_{\varepsilon,h}^{n+1,k+1}, \lambda_{\varepsilon,h}^{n+1,k+1})$
- 10: Stop the  $k$  loop
- 11: **end if**
- 12: **end for**
- 13: **end for**

3.3.2. Strategy II: Newton–Raphson algorithm

We solve the nonlinear problem  $\mathcal{P}_\varepsilon$  by using the Newton–Raphson method to improve the linear convergence rate characterizing the fixed-point algorithm. For the discretization of the material derivative, we use the backward differentiation formula of second order rather than the characteristics method. The scheme is bootstrapped by the initial conditions  $\mathbf{u}^{-1} = \mathbf{u}^0 = \mathbf{u}_0$ , where  $\mathbf{u}^{-1}$  is only a convenient notation. Let  $\chi = (\mathbf{u}; p, \lambda)$  represent the global vector of unknowns where the semicolon symbol separates the primal variable  $\mathbf{u}$  and the Lagrange multipliers  $p$  and  $\lambda$ . For any  $n \geq 1$  and  $i \in \mathcal{N}$ , we compute the variables  $\varphi_i^{n-1}, \psi_i^{n-1}$  and  $\mathbf{u}^{*,n-1}$ . Let  $\mathcal{R}$  denote the global residual vector:

$$\mathcal{R}(\chi) \equiv \begin{pmatrix} \mathcal{R}_u(\mathbf{u}, p, \lambda) \\ \mathcal{R}_p(\mathbf{u}) \\ \mathcal{R}_\lambda(\mathbf{u}) \end{pmatrix} = \begin{pmatrix} \rho \left( \frac{3\mathbf{u} - 4\mathbf{u}^{n-1} + \mathbf{u}^{n-2}}{2\Delta t} + \mathbf{u} \cdot \nabla \mathbf{u} \right) - \text{div } \sigma(\mathbf{u}, p) + \sum_{i \in \mathcal{N}} \delta_{\Gamma_i} \lambda - \sum_{k \in K} \delta_{\Gamma_{N,k}} \bar{p}_k \mathbf{n} \\ \text{div } \mathbf{u} \\ \mathbf{u} - \mathbf{u}^{*,n-1} \end{pmatrix}.$$

After the time discretization, the problem  $\mathcal{P}_\varepsilon$  consists in finding  $\chi^n$  such that  $\mathcal{R}(\chi^n) = \mathbf{0}$ , for any  $n \geq 1$ . The Newton algorithm reduces this problem into a sequence of linear sub-problems. Let  $D\mathcal{R}(\chi)[\delta\chi]$  denote the Fréchet derivative of  $\mathcal{R}$  in the direction  $\delta\chi$ . Given the solution at time  $t^n$ , we compute the solution at  $t^{n+1}$  such that: for any subiteration  $k \geq 0$ ,  $\chi^k$  is known and the problem consists in finding:

$$\chi^{k+1} = \chi^k + \delta\chi^k \quad \text{with } D\mathcal{R}(\chi^k)[\delta\chi^k] = -\mathcal{R}(\chi^k).$$

The starting value  $\chi^0$  is assigned by performing a second order extrapolation of the solution at previous time steps. The method is applied recursively until a stopping criteria based on the computation of the residual is satisfied. In what follows, we drop the subscript  $n$  referring to the time whenever it is clear from the context. We then proceed with the space discretization. The Galerkin scheme of the tangent problem reads:

$$\mathcal{P}_{\varepsilon,h}^{n,k}: \text{ given } \varphi_{i,h}^n, \psi_{i,h}^n \text{ and } \mathbf{u}_h^{*,n}, \forall i \in \mathcal{N};$$

$$\text{ find } \delta\mathbf{u}_{\varepsilon,h}^{n+1,k+1} \in \mathbb{V}_h(\mathbf{u}_b), \delta p_{\varepsilon,h}^{n+1,k+1} \in \mathbb{Q}_h \text{ and } \delta\lambda_{\varepsilon,h}^{n+1,k+1} \in \mathbb{W}_h \text{ such that}$$

$$m\left(\delta \mathbf{u}_{\varepsilon, h}^{n+1, k+1}, \mathbf{v}; \frac{3\rho}{2\Delta t}\right) + c\left(\delta \mathbf{u}_{\varepsilon, h}^{n+1, k+1}, \mathbf{v}; \rho, \mathbf{u}_{\varepsilon, h}^{n+1, k}\right) + a\left(\delta \mathbf{u}_{\varepsilon, h}^{n+1, k+1}, \mathbf{v}; \mu\right) + b\left(\mathbf{v}, \delta p_{\varepsilon, h}^{n+1, k+1}\right) + \sum_{i \in \mathcal{N}} m\left(\delta \lambda_{\varepsilon, h}^{n+1, k+1}, \mathbf{v}; |\nabla \varphi_{i, h}^n| \delta_{\varepsilon}(\varphi_{i, h}^n) (1 - \mathcal{H}_{\varepsilon}(\psi_{i, h}^n))\right) = -\left\langle \mathcal{R}_{\mathbf{u}}\left(\mathbf{u}_{\varepsilon, h}^{n+1, k}, p_{\varepsilon, h}^{n+1, k}, \lambda_{\varepsilon, h}^{n+1, k}\right), \mathbf{v}\right\rangle_{\mathbb{V}'_h, \mathbb{V}_h(\mathbf{0})}, \tag{3.2a}$$

$$b\left(\delta \mathbf{u}_{\varepsilon, h}^{n+1, k+1}, q\right) = -\left\langle \mathcal{R}_p\left(\mathbf{u}_{\varepsilon, h}^{n+1, k}\right), q\right\rangle_{\mathbb{Q}'_h, \mathbb{Q}_h}, \tag{3.2b}$$

$$\sum_{i \in \mathcal{N}} m\left(\delta \mathbf{u}_{\varepsilon, h}^{n+1, k+1}, \mathbf{w}; |\nabla \varphi_{i, h}^n| \delta_{\varepsilon}(\varphi_{i, h}^n) (1 - \mathcal{H}_{\varepsilon}(\psi_{i, h}^n))\right) = -\left\langle \mathcal{R}_{\lambda}\left(\mathbf{u}_{\varepsilon, h}^{n+1, k}\right), \mathbf{w}\right\rangle_{\mathbb{W}'_h, \mathbb{W}_h}, \tag{3.2c}$$

for all  $\mathbf{v} \in \mathbb{V}_h(\mathbf{0})$ ,  $q \in \mathbb{Q}_h$  and  $\mathbf{w} \in \mathbb{W}_h(\mathbf{0})$ . The prime symbol (') stands for the corresponding dual space, and the angle brackets  $\langle \cdot, \cdot \rangle$  represents the dual product.

**Algorithm 2** Damped Newton strategy

```

1: Set Newton tolerance  $\epsilon$ , and let  $\chi_{\varepsilon, h}^0$  be the known initial condition
2: for  $n = 1, \dots, n_{\max} = T/\Delta t$  do
3:   Initialize Newton residual  $\epsilon^{n+1, k} = 2\epsilon$ 
4:   Initialize the velocity by a second order extrapolated prediction  $\mathbf{u}_{\varepsilon, h}^{n+1, -1} = \mathbf{u}_{\varepsilon, h}^{n+1, 0} = 2\mathbf{u}_{\varepsilon, h}^n - \mathbf{u}_{\varepsilon, h}^{n-1}$ 
5:   Compute  $(\varphi_{i, h}^n, \psi_{i, h}^n) \in \mathbb{Q}_h^n, \forall i \in \mathcal{N}$  and  $\mathbf{u}_h^{n*} \in \mathbb{V}_h(\mathbf{u}_b)$ 
6:   for  $k = 1, \dots$  do
7:     Compute  $\delta \chi_{\varepsilon, h}^{n+1, k+1}$  from  $\mathcal{R}_{\varepsilon, h}^{n, k}$ (3.2a-3.2b-3.2c).
8:     Compute step size  $\alpha^{n+1, k+1}$  by backtracking line search.
9:     Update  $\chi_{\varepsilon, h}^{n+1, k+1} = \chi_{\varepsilon, h}^{n+1, k} + \alpha^{n+1, k+1} \delta \chi_{\varepsilon, h}^{n+1, k+1}$ .
10:    Compute Newton residual  $\epsilon^{n+1, k+1} = \left| \mathcal{R}_{\mathbf{u}, h}^{n+1, k+1} \right|_{\mathbb{V}'_h}$ 
11:    if  $\epsilon^{n+1, k+1} < \epsilon_N$  then
12:      Break
13:    end if
14:  end for
15:  Update solution  $\mathbf{u}_{\varepsilon, h}^{n+1} = \mathbf{u}_{\varepsilon, h}^{n+1, k+1}$ .
16: end for

```

3.3.3. Strategy III: damped-Newton algorithm

Although Strategy II features a quadratic convergence and allows more stability compared to Strategy I, it diverges when the starting value is not close enough to the expected solution. Stability issues can arise when  $Re$  becomes relatively large and the flow becomes closer to the turbulent regime. To improve the convergence properties, the initialization of the algorithm is set using a damped-Newton strategy. That consists in adapting the length step using a damping factor  $\alpha^{n, k} \in (0, 1]$  and maintaining the same descent direction of the Newton scheme. The increment reads:

$$\chi^{n, k} = \chi^{n, k-1} + \alpha^{n, k} \delta \chi^{n, k} \quad \left( \alpha^{n, k} = 1 \text{ reduces the strategy to a pure Newton-Raphson algorithm} \right).$$

Hereafter, we briefly describe the algorithm, while a detailed description is available in [48]. Let us consider the space  $\mathbb{S} = \mathbb{V}(\mathbf{u}_b) \times \mathbb{Q} \times H^{-1/2}(\cup_{i \in \mathcal{N}} \Gamma_i)^d$ . Let  $P$  be a non-singular operator which is easy to invert, and it will be used as a non-linear preconditioner. Let us introduce  $F : \chi \mapsto \left| P^{-1} \mathcal{R}(\chi) \right|_{\mathbb{S}}^2$  such that  $P = I$  means that no preconditioner is considered. A line-search subproblem is introduced and it minimizes the function  $f : \alpha \mapsto F(\chi^{n, k} + \alpha \delta \chi^{n, k})$  depending on the damping parameter  $\alpha$ . Its derivative with respect to  $\alpha$  reads:

$$f'(\alpha) = \left\langle F'(\chi + \alpha \delta \chi), \delta \chi \right\rangle_{\mathbb{S}', \mathbb{S}} = 2 \left\langle P^{-1} \mathcal{R}(\chi + \alpha \delta \chi), \mathcal{R}'(\chi + \alpha \delta \chi) P^{-1} \delta \chi \right\rangle_{\mathbb{S}, \mathbb{S}'}$$

A strictly decreasing sequence of the damping parameter is then obtained using a second order recurrence algorithm. We initialize  $\alpha$  to 1 and we set a minimal step length  $\alpha_{\min} = 1/10$ . The backtracking line-search is only required when the solutions at two consecutive time steps are not close enough, for instance, near the peak of systole or in a stenotic case. Strategy III is detailed in Algorithm 2.

3.4. Global strategy and parallel performances

In this section, we investigate the stability of the numerical solver with respect to the flow complexity. In light of the numerical observations, the solution method is adequately stated.

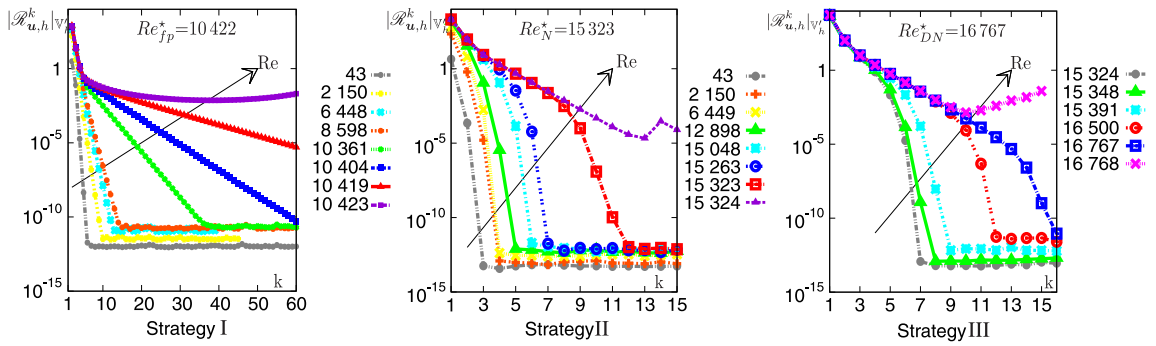


**Fig. 7.** Convergence properties of residuals for several values of the Reynolds number. (left) Results obtained by the fixed-point (FP) algorithm. (middle) Results obtained by the Newton (N) algorithm. (right) Results obtained by the damped-Newton (DN) algorithm.

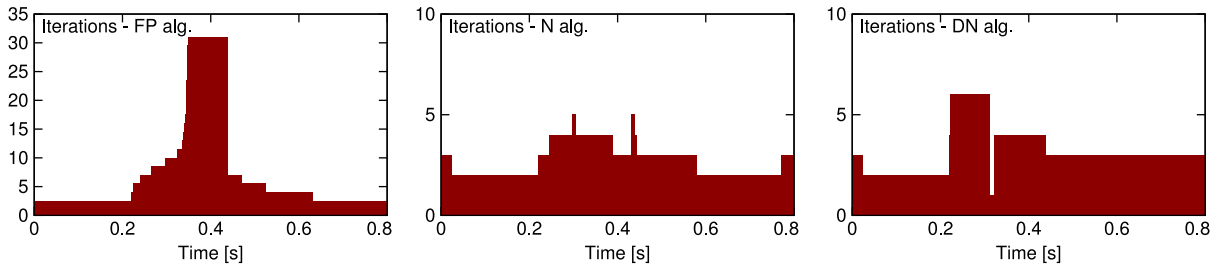


**Fig. 8.** Comparison, in terms of number of iterations, between different strategies over a complete heart cycle.

We consider the valve in the open position and we solve the 3D fluid problem by prescribing the flow rate on  $\Gamma_{in}$  (essential BC) and a fixed pressure equal to  $10^5$  dyn/cm<sup>2</sup> on  $\Gamma_N$  (natural BC). The valve remains in the same position during the entire simulation. To characterize the flow complexity, we evaluate the Reynolds number with respect to the maximal velocity magnitude computed on  $\Gamma_{in}$ .

In what follows, the acronyms FP, N and DN stand for fixed-point, Newton and damped-Newton algorithms, respectively. We denote by  $Re_i^*$  with  $i = fp, N, DN$  the maximum Reynolds number for which a stable solution is obtained when using the fixed-point, Newton or damped-Newton algorithm, respectively.

**3.4.1. Algorithmic strategy**

We proceed with a comparative study of the convergence properties with respect to an increasing value of the flow rate prescribed on  $\Gamma_{in}$ . The residual tracings are plotted in the semi-log scale. Fig. 7 (left) shows the linear convergence behavior of Strategy I. It means that the residual converges exponentially, as expected, with respect to the fixed-point iterations  $k$ . However, the convergence is achieved whenever  $Re$  remains below a specific threshold value  $Re_{fp}^* = 10422$ . For a healthy person, this value can characterize blood flow in the ascending aorta during the systole. In addition, we observe that the number of iterations required to reach the convergence becomes large when  $Re$  increases: almost about 30 iterations for  $Re \approx 10000$ . Accordingly, Strategy I is not beneficial for the simulation of even a mild aortic stenosis because of its high computational cost and its convergence failure.

By using the Strategy II, the quadratic convergence is observed for larger  $Re$ , up to  $Re = 15250$ , see Fig. 7 (middle). Compared to Strategy I, the number of iterations required to reach the convergence is significantly smaller. By increasing  $Re$ , the quadratic convergence is deteriorated until reaching a threshold value  $Re_N^* = 15323$ , beyond it, the algorithm diverges. Fig. 7 (right) shows that the convergence is slightly improved for relatively large  $Re$  when using Strategy III. Indeed, the starting values of the Newton loop become far from the expected solutions when complex flow regimes occur, and the backtracking line-search addresses some convergence issues related to this bad initialization. The corresponding threshold value is  $Re_{DN}^* = 16767$ .

We now consider the simulations over a complete cardiac cycle. Prescribed pressure profiles are imposed on both  $\Gamma_{in}$  and  $\Gamma_{out}$  without solving  $\mathcal{P}_\varepsilon$ . We set the tolerance  $\epsilon_N = 10^{-7}$  and we solve until convergence the problem using the different strategies. Results are depicted in Fig. 8. During the diastole, the number of iterations needed is almost the same for the different strategies. During the systole, Strategy I requires a higher number of iterations, while Strategy II and Strategy III behave similarly. The difference between Strategy II and Strategy III is more pronounced during the systole in the physiological case when  $Re$  becomes much higher, see Fig. 7.

Despite the higher number of sub-iterations usually needed by Strategy I, this strategy remains cheaper in terms of CPU time, see Section 3.4.2. Indeed, the global matrix of the corresponding linear system needs to be assembled only once at each fixed-point loop. Consequently, we always use Strategy I during diastole, whereas Strategy III is used during systole,

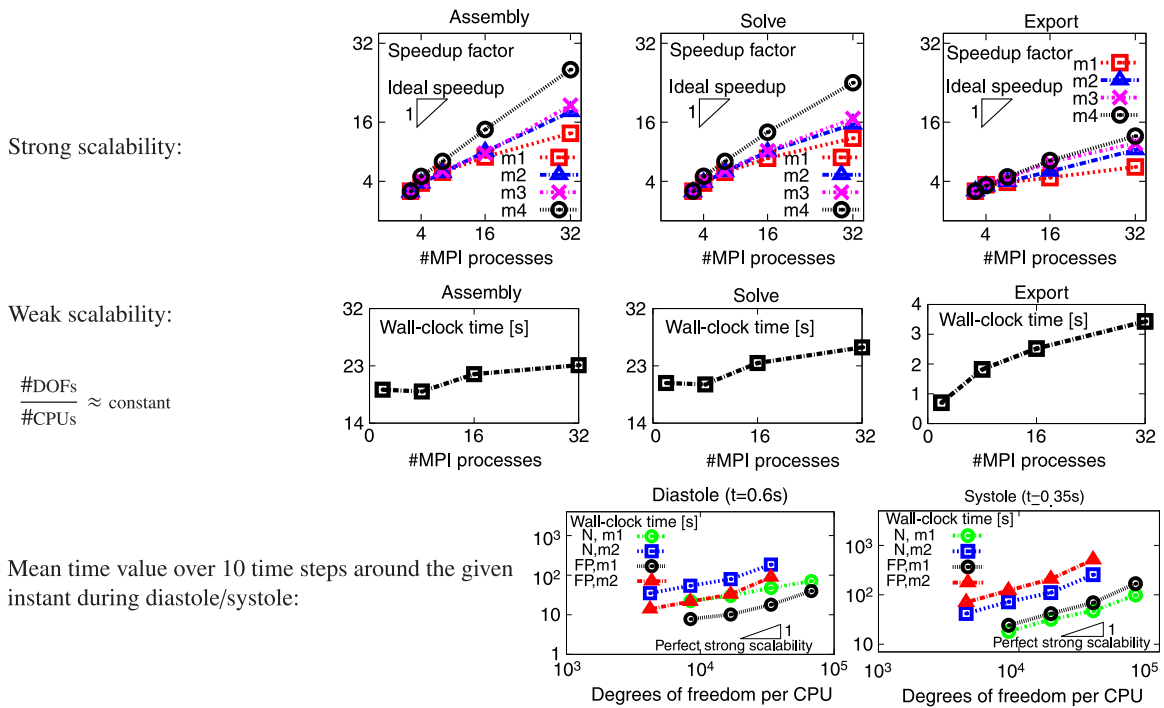


Fig. 9. Numerical investigations of the strong and weak scaling efficiency.

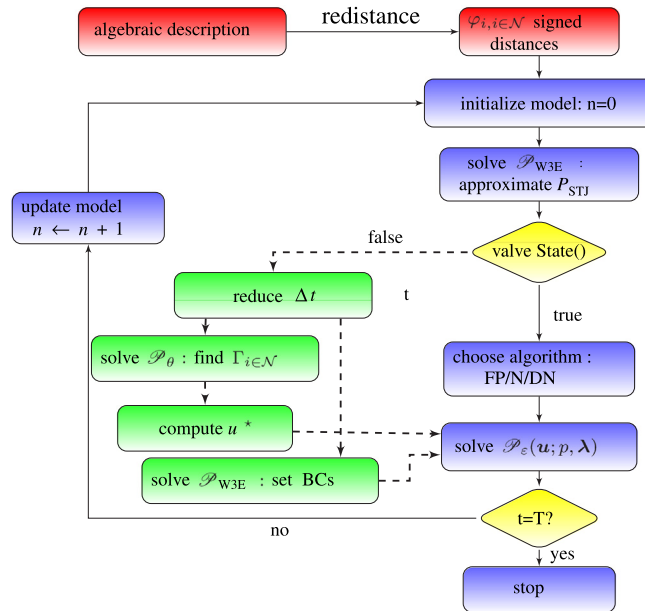


Fig. 10. Graphical illustration of the numerical methodology.

see Fig. 9(bottom). Strategy III is usually reduced to Strategy II during systole, except for a period around the peak of systole and during the deceleration phase. A schematic overview of the structure of the numerical methodology is depicted in Fig. 10.

### 3.4.2. Scalability and parallel performances

To assess the scaling efficiency of the code, we investigate how the computational cost behaves when varying the number of MPI processes or the problem size (degrees of freedom). Each sub-iteration results in three subproblems: the global assembly, the resolution of the linear system and the export of the solution on the hard disk. The performance of the code is measured for these particular subproblems. The speedup  $S = T_p/T_s$  represents a common metric introduced to compare

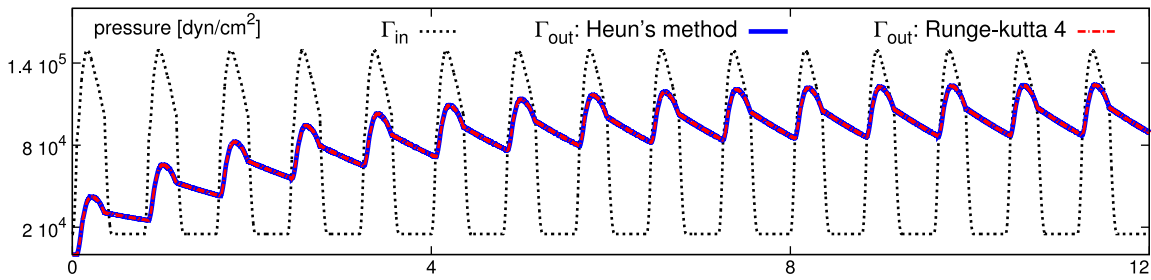


Fig. 11. Temporal evolution of the pressure waveforms obtained with second-order and fourth-order Runge–Kutta methods.

the timing  $T_p$  spent on a parallel architecture to the time  $T_s$  required for a serial execution. The strong and weak scalabilities represent the basic indicators used to characterize the parallel performances depending on whether the architecture is CPU-bound or memory-bound, respectively. The code is strongly scalable if, for the same workload, a two times faster execution is achieved when the number of CPUs is doubled, yielding to a perfect strong scalability equal to one. Remark that the higher the slope is, the more strongly scalable the algorithm is. The code is weakly scalable if, for the same workload per processor, the efficiency remains the same. Perfect weak scalability holds if a perfect overlap of the scalability curves is observed when different meshes are used.

We build several meshes denoted by m1, m2, m3 and m4 and having 42793, 77821, 128420 and 249578 tetrahedral elements, respectively. The scalability results are displayed in Fig. 9. The evolution of the speedup with respect to the MPI processes shows that the global assembly and the resolution phases are almost perfectly scalable, since the different slopes are close to the optimal linear slope. For coarser meshes, the speedup is deteriorated when the number of processors increases. Indeed, more time is needed for the communications between processors rather than for computations. The strong scalability is not as good when exporting results on the hard disk. Improvements in terms of preconditioners and input and output timings are needed.

To study the weak scalability, different meshes are built while keeping almost the same problem size per processor. In the second row of Fig. 9, good weak scaling properties are observed for the assembly, less good but acceptable properties are observed for the resolution, whereas poor weak scalability is observed for data saving.

We now investigate the scalability of Strategy I and Strategy II during diastole and systole. We display the mean value of the computing times over ten time iterations, with respect to the degrees of freedom per CPU. The slopes of the different curves are close to the linear slope, showing acceptable strong and weak scaling. Since the assembly of the linear system is performed once at each time step, Strategy I is clearly more beneficial than Strategy II during diastole in which the two strategies require almost a similar number of iterations until convergence, see Fig. 8.

### 3.5. Numerical approximation of the Windkessel model

We briefly describe the numerical approach used to solve the three-element Windkessel model  $\mathcal{P}_{W3E}$  (2.4). The flow rate is first computed after solving the fluid problem ((2.1)–(2.2)–(2.3)). The second-order ordinary differential equation is converted into two first-order ordinary differential equations. Several numerical methods can be used to solve the resulting initial value problem such as the Taylor series method, the linear multistep methods and the Runge–Kutta methods. We refer to [49] for a detailed description of these methods.

In the present work, we consider a two-stage second-order Runge–Kutta method, also known as Heun’s method. The discretized problem is recursively solved in time. Given the flow rate  $Q^{n+1}$ , we compute  $\bar{p}^{n+1}$  such that:

$$CR_d \frac{\tilde{p}_*^{n+1} - p_*^n}{\Delta t} + p_*^n = R_d Q^{n+1},$$

$$CR_d \frac{p_*^{n+1} - p_*^n}{\Delta t} + \frac{\tilde{p}_*^{n+1} + p_*^n}{2} = R_d Q^{n+1},$$

$$\bar{p}^{n+1} = R_p Q^{n+1} + p_*^{n+1}.$$

Let us consider a mesh having 21,793 tetrahedra and we set  $\Delta t = 10^{-3}$ . We consider a simplified diode-like model for the dynamics of the valve which consists in switching the leaflets between the fully open and fully close positions without modeling the intermediate positions. A periodic left ventricular pressure is prescribed on the upstream boundary and we solve  $\mathcal{P}_{W3E}$  (2.4) until reaching a fully periodic regime. The parameters of the lumped model are tuned and are given by  $R_p = 170 \text{ dyn s cm}^{-5}$ ,  $R_d = 3000 \text{ dyn s cm}^{-5}$  and  $C = 8 \times 10^{-4} \text{ cm}^5 \text{ dyn}^{-1}$ . Fig. 11 compares the temporal evolution of the pressure on  $\Gamma_{out}$  with the the solution obtained by a more sophisticated fourth-order Runge–Kutta method using the same model parameters. Results show that the pressure curves obtained by the two methods are almost indistinguishable. In what follows, we use the second-order Runge–Kutta method.

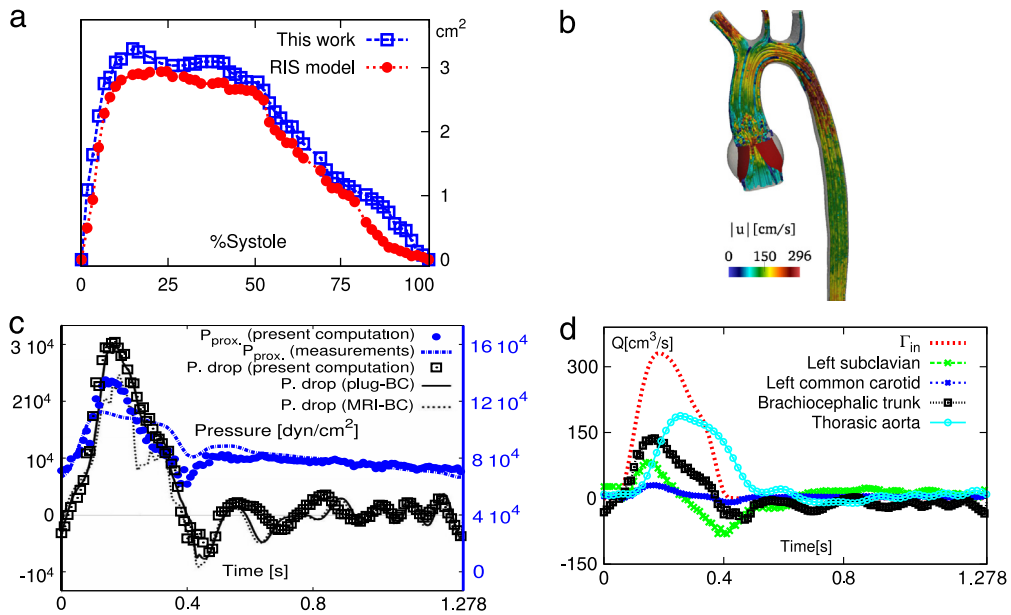


**Fig. 12.** Example 1. (a) Temporal changes in the EOA during systole and comparison with the RIS model. (b) Streamlines with color-coded velocity magnitude at peak systole. (c) Comparisons to measurements [51] and available results [52] of the proximal pressure to AoC and the pressure drop across the AoC. (d) Imposed or computed flow rates at different boundaries. (For interpretation of the references to color in this figure legend, the reader is referred to the web version of this article.)

#### 4. Numerical examples and cardiovascular simulations

In what follows, we provide a set of numerical examples in both two-dimensional and three-dimensional cases to test the performance of the finite element method described above. In Example 1, we present a validation of our method by performing comparisons with other numerical and experimental results. The method is tested in the two-dimensional case in Example 2. Physiologically relevant computations are provided for both healthy and pathological valves in Example 3. We perform simulations in the full aorta and sinus of Valsalva in Example 4. Finally, we investigate the incidence of flow stagnation after TAVI in Example 5.

*Software implementation.* The presented method has been implemented using the C++ library for scientific computing Rheolef [50]. Rheolef provides support for distributed-memory parallelism via MPI<sup>7</sup> and relies upon the Boost,<sup>8</sup> Blas,<sup>9</sup> Scotch,<sup>10</sup> and UMFPACK<sup>11</sup> libraries for much of its functionalities. Results are displayed graphically using the softwares Paraview<sup>12</sup> and Gnuplot.<sup>13</sup>

##### 4.1. Example 1: model validation

The purpose of this example is twofold. A numerical validation is first obtained by comparing our computational results to those obtained by the RIS model. A clinical validation is performed subsequently in the case of patient-specific thoracic aortic coarctation.

##### 4.1.1. Numerical validation versus the RIS model

We first perform a numerical validation by comparing our results with the results obtained by the RIS method while considering only the fully open or closed positions of the valve, as introduced in [6]. The RIS method was previously validated with respect to a reference simulation based on a 3D-FSI model, where the evaluation of the effective orifice area, referred to as EOA, is adopted for the comparisons [6]. The EOA is a clinical index measured by transthoracic echocardiography and

<sup>7</sup> Message Passing Interface—<http://www.mpich.org>.

<sup>8</sup> Boost libraries—<http://www.boost.org>.

<sup>9</sup> Basic Linear Algebra Subprograms library—<http://www.netlib.org/blas>.

<sup>10</sup> Scotch—<http://www.labri.fr/perso/pelegrin/scotch>.

<sup>11</sup> Umfpack routines—<http://www.cise.ufl.edu/research/sparse/umfpack/>.

<sup>12</sup> Paraview—<http://www.paraview.org>.

<sup>13</sup> Gnuplot—<http://www.gnuplot.info>.

**Table 1**

Example 1. Convergence study showing the computed flow rates (in L/min) at different boundaries for several values of the time step size.

	$\Delta t = 5 \times 10^{-2}$	$\Delta t = 10^{-2}$	$\Delta t = 5 \times 10^{-3}$	$\Delta t = 10^{-3}$
Brachiocephalic trunk	0.637	0.654	0.656	0.656
Left common carotid artery	0.489	0.331	0.309	0.302
Left subclavian artery	0.291	0.317	0.328	0.334
Descending aorta	2.304	2.419	2.428	2.429

**Table 2**

Example 1. Average mass flow (in L/min), pressure drop through the coarctation (in dyn/cm<sup>2</sup>) and comparison with measurements and other studies through the various branches of the aortic model under rest conditions.

	Measurements	Computations	Errors	BC1 [51]	BC5 [51]
Total flow at brachiocephalic trunk	0.624	0.656	5.13%	0.65	1.01
Total flow at left common carotid artery	0.312	0.302	3.21%	0.31	0.17
Total flow at left subclavian artery	0.364	0.334	8.24%	0.38	0.19
Total flow at descending aorta	2.41	2.429	0.79%	0.49	2.46
Average pressure at coarctation	$8.45 \times 10^4$	$8.28 \times 10^4$	2.01%	$6.96 \times 10^4$	$8.00 \times 10^4$
Proximal systolic pressure at coarctation	$1.12 \times 10^5$	$1.34 \times 10^5$	19.64%	$9.00 \times 10^5$	$1.41 \times 10^5$

frequently used to quantify the AS severity [53]. We adopt the temporal changes in the EOA during systole as a comparison criterion, as it provides incremental prognostic information beyond what is obtained for the standard EOA [53]. It expresses the ratio between the instantaneous flow and the instantaneous maximal velocity of the transvalvular flow [53].

We use the same setup of a healthy valve as described in Example 3 (4.3) in which  $\Omega$  represents the sinus of Valsalva. We report the results when the fully periodic regime is established. The cardiac output is 4.69 L/min, the heart rate is 75 beats/min and the systole represents 29.1% of the heart cycle. The mean arterial and peak systolic pressures are  $8.9 \times 10^4$  dyn/cm<sup>2</sup> and  $1.15 \times 10^5$  dyn/cm<sup>2</sup>, respectively. Fig. 12(c) shows a good agreement between the numerical results obtained by the present method and the RIS method.

#### 4.1.2. Clinical validation of a patient-specific thoracic aortic coarctation model

We investigate a patient-specific hemodynamics at rest of a 17-year old subject with a mild thoracic aortic coarctation (AoC) (45% degree of stenosis with a minimal diameter of 10 mm). The aorta is characterized by a reduction in luminal cross-section which results in high pressure gradient across the coarctation. The anatomical model was provided in the STACOM 2013 [51], where a Gadolinium-based contrast agent MR angiography was realized with the patient in the supine position inside a 1.5-T Phillips scanner. Hemodynamic data at rest conditions were obtained using a phase-contrast magnetic resonance imaging (cardiac-gated, 2D, respiratory compensated, phase-contrast cine sequence with through-plane velocity encoding). The cardiac output of the patient increased to 3.71 L/min and the heart rate is 47 beats per minute.

In this example, essential boundary conditions are prescribed on the inlet and thoracic aorta. We set essential boundary conditions based on the Fourier reconstruction of the flow waveforms on  $\Gamma_{in}$  and diaphragmatic aorta. Remark that the flow rate on  $\Gamma_{in}$  is forced to zero during diastole. The Windkessel model allows to compute the pressure waveforms imposed subsequently as natural boundary conditions on the supra-aortic vessels. The temporal evolution of the computed flow waveforms is depicted in Fig. 12(d). A time step sensitivity study is provided in Table 1, showing minor changes for the time steps  $\Delta t$  smaller than  $10^{-2}$ . In Table 2, we perform a quantitative comparison of our computational results with respect to the clinical measurements and some numerical results available in the literature [51], where BC1 and BC5 stand for particular boundary conditions described in [51]. We also provide the relative errors between our results and the clinical measurements. We observe particularly the total flow through the supra-aortic branches and the diaphragmatic section of the aorta. A satisfactory agreement is observed overall.

We also study the pressure gradient through the aortic coarctation and we perform comparison with the invasive pressure wire measurements acquired in a catheterization laboratory-equipped XMR suite [51]. For this purpose, we define the proximal plane by the point (188.96, 40.18, 253.22) and the normal vector (0.98, -0.09, -0.19), while the distal plane is characterized by the point (261.97, 23.56, 277.10) and the normal vector (0.99, -0.03, -0.14). We evaluate the pressure gradient across the AoC as the pressure gradient between the proximal and distal planes. In Fig. 12(c), a comparison between the computed proximal pressure and the 15-mode Fourier reconstruction of the measured pressure shows good agreement during the ES, LS and diastole, whereas the maximal mismatch is observed around the PS. However, our numerical results are comparable to those obtained in [51].

Fig. 12(c) shows a close fit of the simulated pressure gradient with respect to the computations reported in [52], in which different sets of boundary conditions, referred to as “plug” and “MRI-based”, are considered.

#### 4.2. Example 2: two-dimensional test case

Although the aortic flow is inherently three-dimensional, the two-dimensional problem enables to highlight several features of the model, and helps to test the reduced order model used to follow the movement of the valve. The setup reads

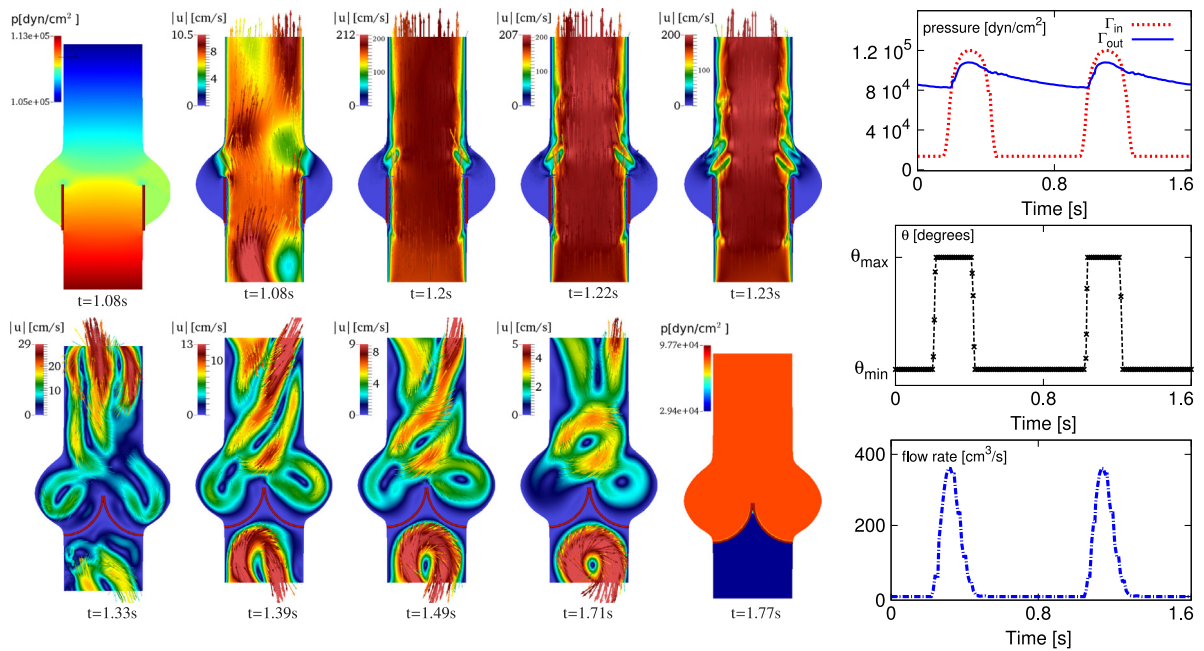


**Fig. 13.** Example 2. (left) Snapshots showing the velocity and pressure profiles during the cardiac cycle. (right) Temporal evolution of the mean pressure on inlet  $\Gamma_{in}$  and outlet  $\Gamma_{out}$ , the valve opening angle  $\theta$  and the flow rate measured on  $\Gamma_{in}$ .

as follows: a simplified fluid domain was extracted from the published literature [43], see Fig. 4. The initial mesh possesses 117,786 triangular elements almost regular (element radii ratio larger than 0.65 for all elements). The fluid density and viscosity are  $\rho = 1 \text{ g/cm}^3$  and  $\mu = 0.035 \text{ g/cm} \cdot \text{s}$ . The fluid is initially at rest and the time step size is  $\Delta t = 5 \times 10^{-3} \text{ s}$ . The three-element Windkessel problem is disregarded, and we rather prescribe the upstream and downstream pressure profiles. The valve opening angle is obtained by solving  $\mathcal{P}_\theta$ , see Fig. 13.

Snapshots of the velocity and pressure profiles are displayed in Fig. 13. A positive pressure gradient across the valve induces the leaflets opening. Hence, a forward flow is observed and an acceleration phase characterizes the ejected flow until the peak of systole where the maximum ejection velocity is 212 cm/s. The peak of systole corresponds to the largest pressure gradient across the valve. The accelerating blood flow looks more stable during this phase than during the deceleration phase, see snapshots at  $t = 1.2 \text{ s}$  and  $t = 1.23 \text{ s}$ . The temporal evolution of the flow rate on  $\Gamma_{out}$  is provided in Fig. 13 (right). During diastole, the valve is subjected to a high pressure jump, see Fig. 13 at  $t = 1.77 \text{ s}$ . The closure of the valve is triggered by the flow reversal in the opposite direction to the valve opening. The flow exhibits a complex vortical behavior triggered by the fast closure of the leaflets and the backward movement of aortic flow into the sinuses. Several flow recirculations are then observed, see snapshots at  $t \in \{1.33, 1.39, 1.49, 1.71\} \text{ s}$ .

#### 4.3. Example 3: three-dimensional simulations in the sinus of Valsalva with healthy and stenotic valves

The aims of this example are twofold. On the one hand, we perform computations in full 3D. On the other hand, we investigate the model in physiologically relevant conditions with healthy and stenotic valves. In this regard, a realistic and periodic left-ventricular pressure waveform is imposed on  $\Gamma_{in}$ , see Fig. 14, while the three-element Windkessel model enables to account for the cumulative effects of the distal aorta and vessels. Physiological aortic loading pressure is obtained by tuning the model parameters, given by  $R_p = 150 \text{ dyn s/cm}^5$ ,  $R_d = 4000 \text{ dyn s/cm}^5$  and  $C = 5 \times 10^{-4} \text{ cm}^5/\text{dyn}$ . We set  $\Delta t = 10^{-3} \text{ s}$  and we run the simulation for several heart cycles until a periodic pressure waveform is obtained on  $\Gamma_{out}$  (almost after six heartbeats), see Fig. 14.

When the fully periodic regime is established, we plot in Fig. 15 the instantaneous velocity magnitude and velocity field at a cross-section located downstream of the aortic valve. Snapshots provide a comparison between the profiles obtained at corresponding times in two successive periods  $T_8^*$  and  $T_9^*$ . By visual inspection, we could recognize similar flow patterns, while small discrepancies are observed in the early diastole. Indeed, that is due to the strong reversal flow which triggers the valve closure.

Multiple clinically relevant parameters such as systolic, diastolic and mean pressure gradient help diagnostically to identify healthy cases. The mean pressure gradient represents the integrated pressure gradient between the left ventricular and the aortic pressures throughout the systole. Small values of the mean pressure gradient characterize a healthy valve with a very small resistance to flow, while high values characterize the severity of the aortic stenosis. The transvalvular mean pressure gradient is represented by the shaded blue area in Fig. 14. That is about  $7219 \text{ dyn/cm}^2$  and is within the

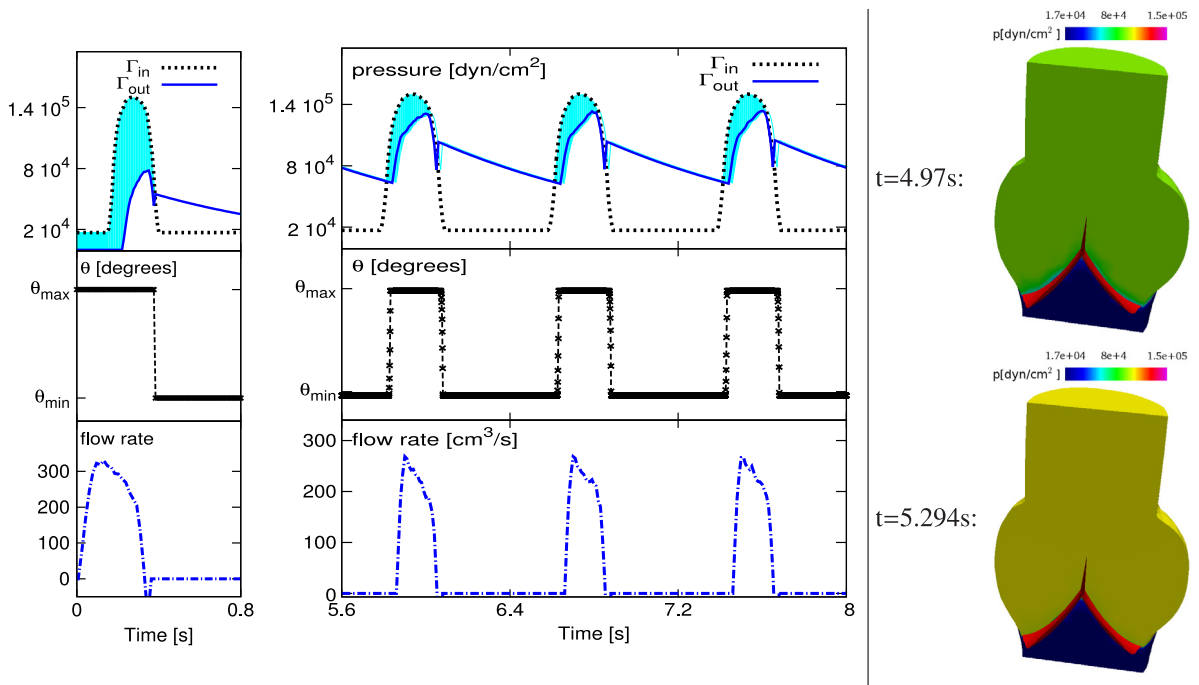


**Fig. 14.** Example 3. Multibeat simulations with a healthy aortic valve. Left-Middle: Temporal evolution of the hemodynamical quantities. Right: Snapshots showing the pressure profiles. (For interpretation of the references to color in this figure legend, the reader is referred to the web version of this article.)

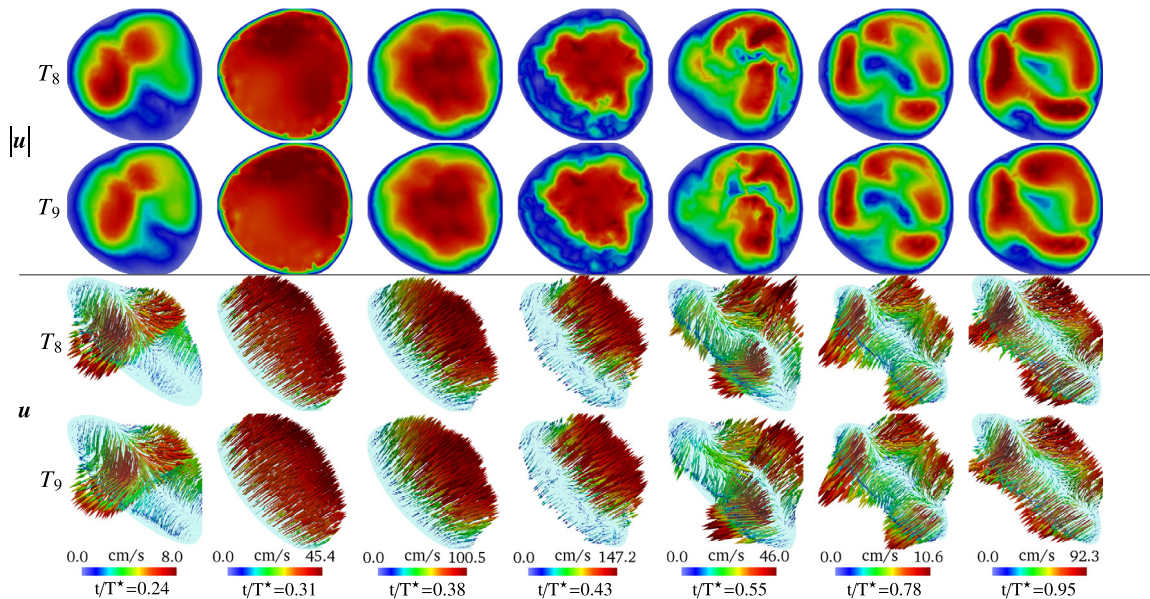


**Fig. 15.** Example 3. Cross-section velocity profiles at the same time for successive periods when the fully periodic regime is established.

physiological range of values  $[0, 13\ 300]$  dyn/cm<sup>2</sup> as reported in.<sup>14</sup> In addition, the peak instantaneous pressure gradient behaves as the mean pressure gradient and measures the peak of the difference between the left ventricular and the aortic pressures. During the seventh heartbeat, this peak is about 70 778 dyn/cm<sup>2</sup> and is reached at  $t = 5.06$  s. When the periodic regime is fully established, the diastolic pressure is obtained at early systole and is approximately equal to  $6.4 \times 10^4$  dyn/cm<sup>2</sup>. The pressure increases as blood flows into the ascending aorta, and the maximum systolic pressure is about  $1.35 \times 10^5$  dyn/cm<sup>2</sup>. The aortic pulse pressure is approximately  $7.1 \times 10^4$  dyn/cm<sup>2</sup>; it represents the maximum

<sup>14</sup> <http://www.clevelandclinicmeded.com>.

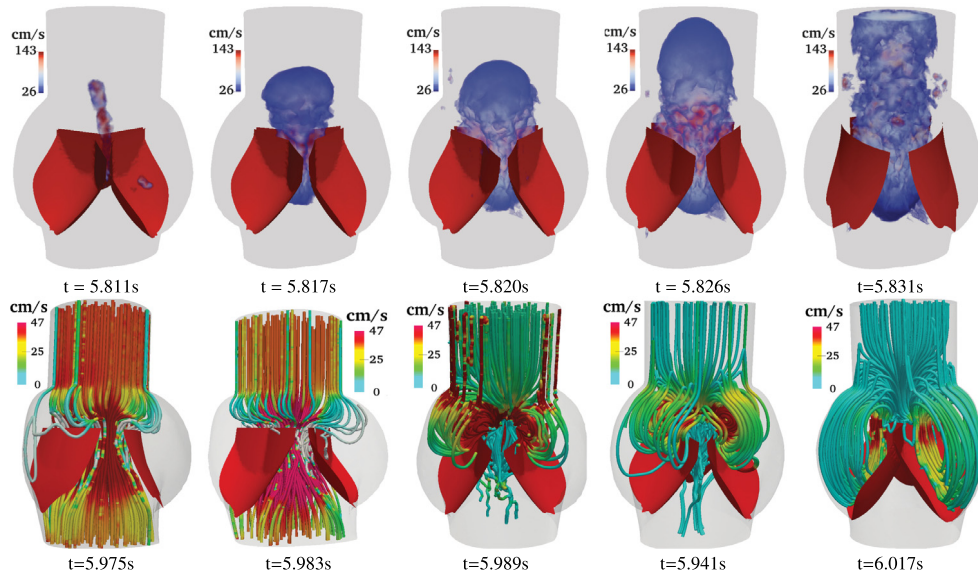


**Fig. 16.** Example 3. Top: Opening of healthy AV at early systole; Volume-rendered blood velocity magnitude. Bottom: Closure of healthy AV at late systole; Streamlines showing the vortical flow patterns which trigger the valve closing.

change in the aortic pressure during systole and is given by the difference between the systolic and the diastolic pressure. Note that the pulse pressure is slightly higher than the experimentally obtained value of about 40 mmHg. This difference can be related to the unphysiological stiffness of the aorta, since a highly compliant aorta has a smaller pulse pressure. Thereafter, a deceleration phase starts and the pressure falls until the aortic pressure becomes equal to the left ventricular pressure. The systolic phase lasts about 0.235 s before the closure of the aortic valve. The aortic pressure continues decreasing until a new cardiac cycle starts. We provide in Fig. 14 snapshots of the pressure distribution in the longitudinal mid surface of the SV during diastole, showing mainly the ability of the model to capture the sharp pressure jump across the fully closed leaflets.

The temporal evolution of the angle  $\theta$  computed by the lumped parameter model  $\mathcal{P}_\theta$  is plotted in Fig. 14. Snapshots showing the leaflets' shapes during the opening and closing phases are provided in Fig. 6. Remark that only few positions, almost between five and ten, are captured in general during the opening and closing phases. The volumetric flow rate wave is also depicted in Fig. 14.

After simulating seven cardiac cycles, the periodic regime is established and the peak systole is reached at  $t = 5.09$  s. The peak flow rate is approximately  $271.4 \text{ cm}^3/\text{s}$ . Throughout similar studies, this value is within the physiological range. The peak flow rate reported in [6] is about  $180 \text{ cm}^3/\text{s}$ , whereas the corresponding value reported in [27] is about  $420 \text{ cm}^3/\text{s}$ . Snapshots showing the flow profile near the healthy AV in early and late systole are provided in Fig. 16. The peak systolic velocity corresponds to the maximal flow ejection and is about  $150 \text{ cm/s}$ . During the deceleration phase, a more complex flow dynamics holds, see streamlines in Fig. 16. Vortices start on the top of the valvular free-edges, and recirculations trigger the fast closure of the leaflets. Big vortices are subsequently developed inside the sinuses and allow to keep the valve closed during diastole.

Thereafter, we aim to assess the ability of the model to characterize pathological valves. To model the calcific aortic stenosis, we restrict the maximum opening angle of the diseased cusps to  $\theta_{\max}^* = 59^\circ$  (to mimic the narrowing), see Fig. 17. That corresponds to  $\mathcal{E} \in [0, 0.65]$ . The prescribed left ventricular pressure and the computed aortic pressure tracings reveal an elevated transvalvular pressure gradient, see the shaded blue area in Fig. 17. In addition, the peak instantaneous pressure gradient is almost about  $74998 \text{ dyn/cm}^2 \in [33325, 79980] \text{ dyn/cm}^2$ , characterizing consequently a moderate aortic stenosis. The diastolic and systolic pressures are about  $4.49 \times 10^4 \text{ dyn/cm}^2$  and  $8.99 \times 10^4 \text{ dyn/cm}^2$ , respectively. The aortic pulse pressure is about  $4.5 \times 10^4 \text{ dyn/cm}^2$  and is larger than the one corresponding to the healthy valve. Some snapshots showing the fluid dynamics during the systole when the stenotic valve is fully open are provided in Fig. 17. The effect of the stenosis on the jet profile across the valve is remarkable and the maximum flow rate is now about  $431.7 \text{ cm}^3/\text{s}$ . Since the narrowed valve results in an increase of the fluid velocity through the valve, the assessment of the severity of the stenosis can also be diagnosed by the aortic velocity [54]. Numerically, the maximum jet is characterized by a maximal velocity almost equal to  $350 \text{ cm/s}$ . Streamlines in Fig. 17 show that the fluid exhibits a more complex three-dimensional pattern compared to the healthy case.

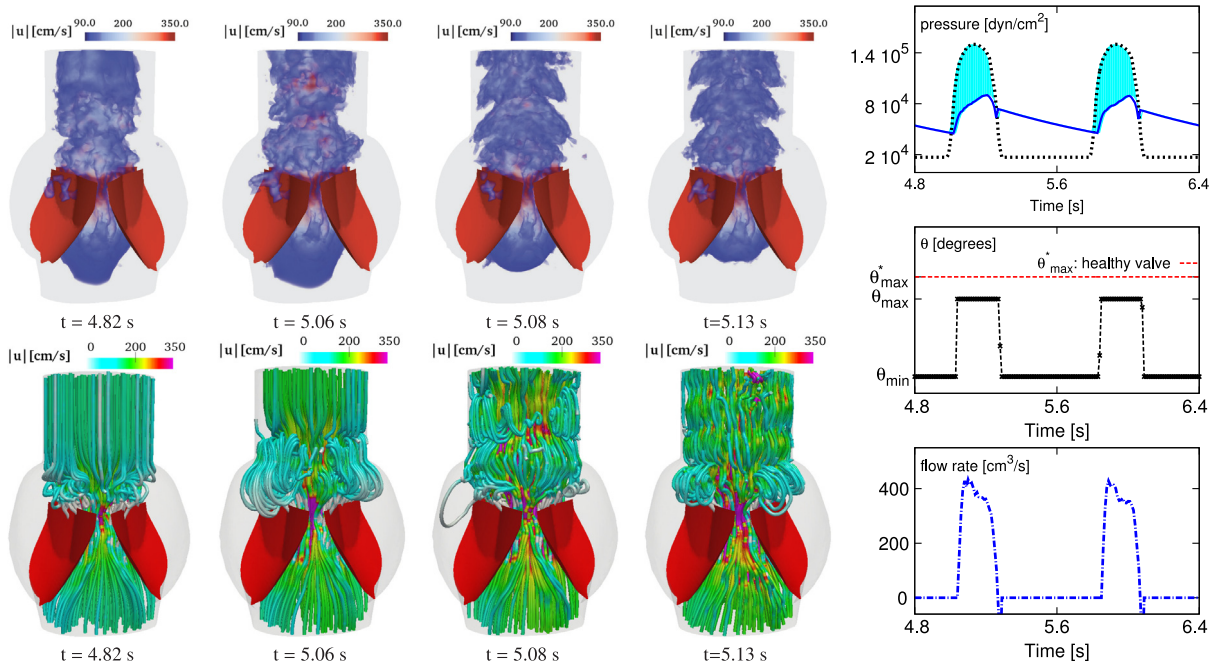


**Fig. 17.** Example 3. Stenotic aortic valve during systole. Left-Top: Volume-rendered blood flow velocity magnitude. Left-Bottom: Streamlines showing complex flow pattern. Right: Temporal evolution of hemodynamical quantities when the fully periodic regime is established. (For interpretation of the references to color in this figure legend, the reader is referred to the web version of this article.)

**Table 3**

Example 4. Tuned parameters for the Windkessel model and averaged/maximal computed flow rates over the eighth heart cycle at the outlets of the computational domain.

Outlet	$R_p$ [dyn s/cm <sup>5</sup> ]	$R_d$ [dyn s/cm <sup>5</sup> ]	$C$ [cm <sup>5</sup> /dyn]	Mean fluxes (cm <sup>3</sup> /s)	Maximal fluxes (cm <sup>3</sup> /s)
Brachiocephalic trunk	412.70	9179.32	$2.6 \times 10^{-4}$	8.79	69.09
Left common carotid artery	648.40	90 335.80	$1.05 \times 10^{-4}$	5.03	35.21
Left subclavian artery	556.10	62 100.00	$3.12 \times 10^{-4}$	6.96	47.06
Descending thoracic aorta	133.54	1445.70	$1.08 \times 10^{-3}$	59.62	258.50

#### 4.4. Example 4: three-dimensional fluid dynamics in the full aorta and sinus of Valsalva

This test case concerns the simulation of blood flow in the aorta and sinus of Valsalva. Some particular points labelled respectively by A, B, C and D are highlighted on the surface of the aorta, see Fig. 18. Two numerical experiments are performed considering healthy and stenotic valves, respectively. In the stenotic case, only one leaflet is assumed diseased while the two other leaflets behave healthy. The point B in Fig. 18 is placed on the sinotubular junction and is faced by the diseased leaflet in the second experiment. From a medical viewpoint, this configuration is possible since the calcification can affect the leaflets in different manners [6]. That also shows the flexibility of the present model to consider less usual configurations. A complex flow dynamics is expected due to the non-planarity and the curvature of the aorta, the movement of the leaflets, and the non-symmetric configuration of the leaflets and the sinuses.

The nomenclature used for the geometry and the different outlets is provided in Fig. 18. The outer boundaries include the descending thoracic aorta and the three upper branch vessels: the brachiocephalic trunk, the left common carotid artery and the left subclavian artery. The numerical test is set as follows: a time-varying left ventricular pressure is prescribed on the inlet, while the parameters of the three-element Windkessel model are tuned such that physiologically meaningful pressure waveforms are set on the outer boundaries. The tuned parameters are depicted in Table 3. In the healthy case, the averaged and maximal fluxes at each outlets are also summarized in Table 3. We particularly observe that about 63% of blood travelling across the healthy aortic valve is ejected through the descending thoracic aorta during systole. The prescribed inner pressure and the computed pressure waveforms on the remaining boundaries are displayed in Fig. 18. The time evolution of the computed flow rates, the opening angle of the healthy valve and the averaged pressure computed on the sinotubular junction are also depicted.

Let the acronyms ES, PS, LS and MD stand for early systole, peak systole, late systole and mid-diastole, respectively. When the periodic regime is established, the distribution of AWSS, OSI and WSS at PS, LS and MD are depicted in Fig. 20. Results show that high values of the WSS are observed in the aortic arch. That comes from the jet created during systole and the

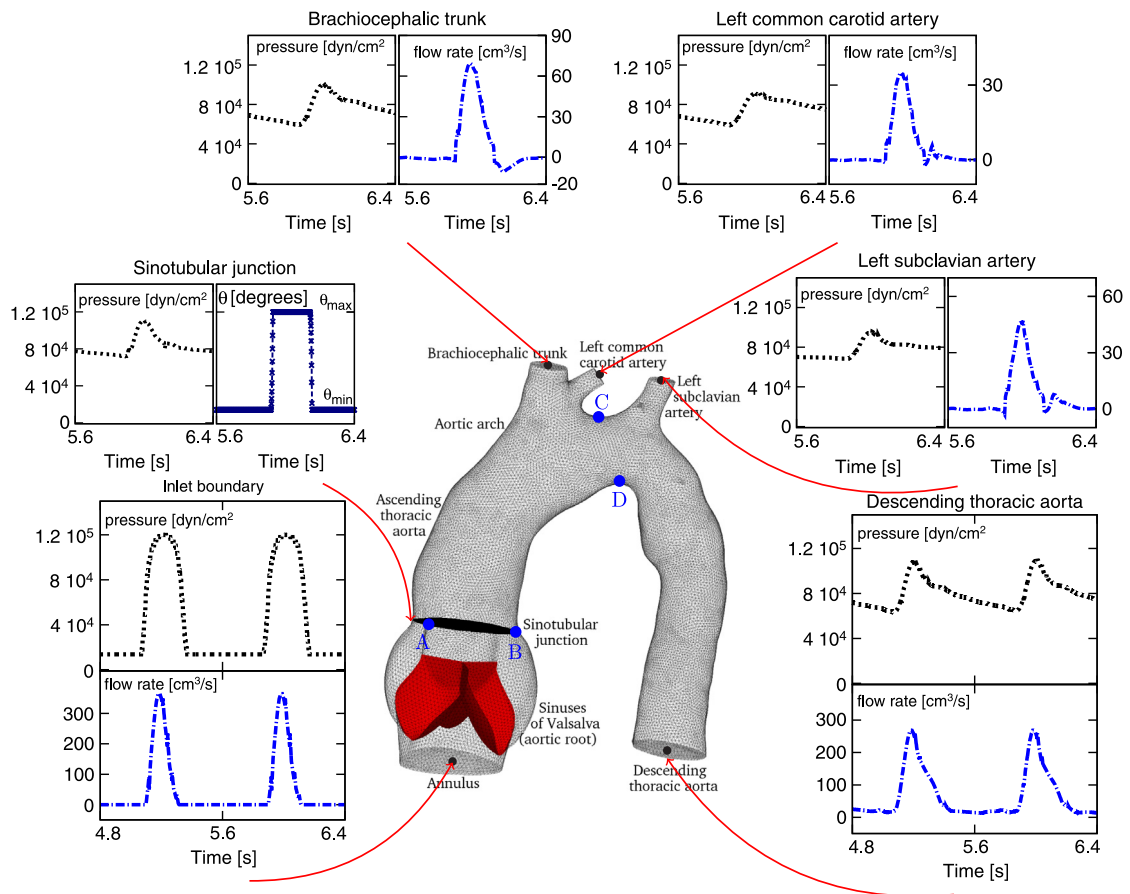


**Fig. 18.** Example 4. Fluid dynamics in the full aorta and SV. Nomenclature and computed pressure and flow rates at different boundaries.

reversal flow occurring in the left subclavian artery during diastole. In addition, high WSS is reported in the upper branch vessels especially at PS and MD where high flow is ejected through these arteries. We also see that the WSS in the descending aorta is important especially in the stenotic case where blood becomes more strongly ejected. Notice that a big area in the ascending aorta and SV becomes also subjected to a high sustained WSS in the stenotic case during the systole.

This is due to the large velocity gradient which is mainly created during the acceleration phase of the systole. Since the high jet is oriented toward the region A, the tracing of the WSS time history in this location indicates that the WSS is enhanced by almost a factor of 40 during some periods of the heart cycle in the diseased case.

The AWSS distribution obviously reveals that the stenotic case is subject to larger values of WSS in the areas outlined above. Some snapshots of the streamlines are provided in Fig. 19. Regarding the OSI pattern, Fig. 20 shows small values, almost zero, particularly in the descending aorta because of the positive outflow observed in this branch in both systole and diastole. Since the upper branch arteries experienced high retrograde flow during diastole, the OSI is close to 0.5. Moreover, high values of OSI are observed in the ascending aorta since complex flow recirculations hold in this region during diastole. Helical flow pattern is clearly observed in Fig. 19 at MD.

#### 4.5. Example 5: potential flow stagnation after transcatheter aortic valve implantation

We consider the same setup described in Example (4.2) (2D case) and Example (4.2) (3D case). We thereafter undertook a numerical investigation to assess the implications of TAVI on the fluid dynamics. As an approximation, the heavily calcified cusps are assumed fully rigid in the open position, yielding the no slip condition  $\mathbf{u} = \mathbf{0}$  for the fluid on the leaflets. Although the calcified leaflets are usually remodeled and their shapes do not look like the healthy shapes, we assume in this preliminary work that leaflets remain thin. We investigate the flow dynamics with respect to the area of the calcified surface. Indeed, we examine the hemodynamical repercussion in the SV with respect to the area A of the calcified cusp ( $A = 0$  simply corresponds to the case of a healthy valve). A noticeable consequence is that after TAVI, the presence of both old and implanted valves causes a strong effect on blood flow patterns, see Fig. 21. In fact, the blood velocity decreases significantly in the lower parts of the sinuses after TAVI, creating consequently low flow zones. Such dead zones are characterized by low shear rate magnitude  $\dot{\gamma}$  wherein blood flow stagnates and may coagulate in a threshold-like manner [55]. Since the

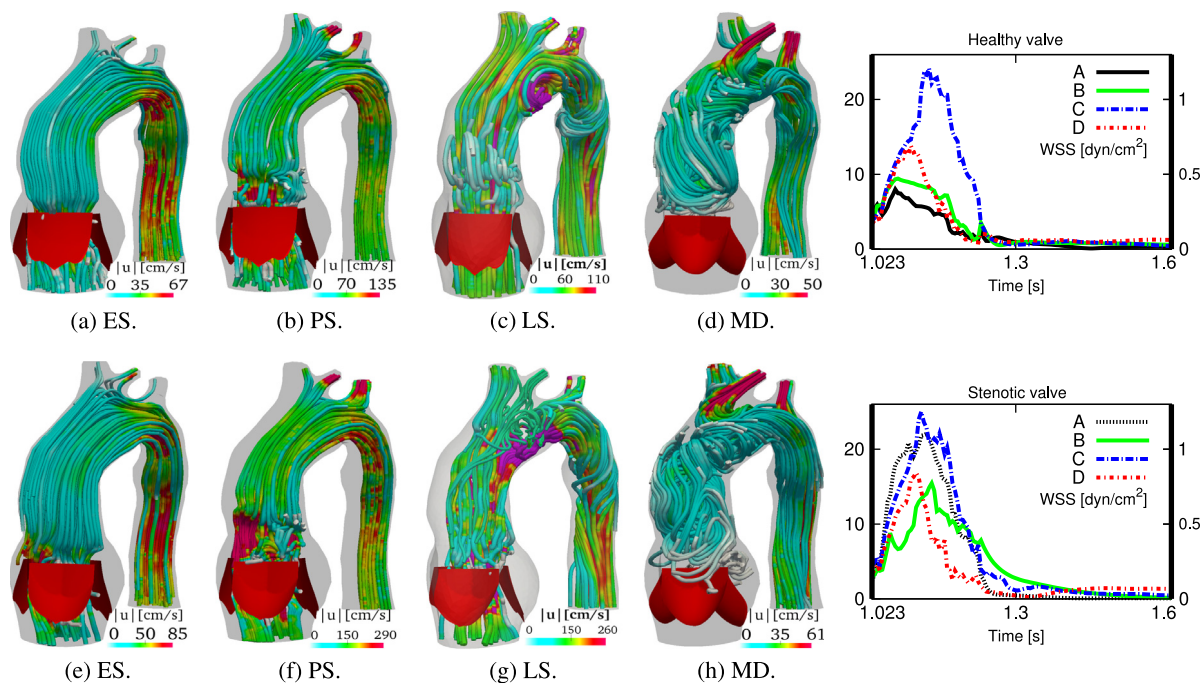


**Fig. 19.** Example 4. Top row: Healthy aortic valve. Bottom row: Stenotic aortic valve. Right: Streamlines. Left: Time history of WSS magnitude at particular positions. The legends of the continuous and discontinuous lines are depicted in the right and left panels, respectively.

shear rate governs the advection phenomena near the walls [56], it represents a better indicator of potential thrombosis than either velocity or flux. To characterize the stagnation, we measure the “stagnation volume” (stagnation area in 2D) that represents the volume (area in 2D) of the zone where  $\dot{\gamma}$  is small enough to favor stagnation (below a threshold value  $5 \text{ s}^{-1}$ ). Snapshots in Fig. 21 show that the stagnant regions (white-colored) of low flow  $\mathbf{u} \leq 0.1 \text{ cm/s}$  and low shear rate  $\dot{\gamma} \leq 5 \text{ s}^{-1}$  are created after TAVI in the bottom of the sinuses. However, such dead zones are not observed in the healthy case.

Our current intuitive understanding is as follows. In the healthy case, the leaflets quickly open under the action of the pressure gradient and blood particles are strongly pushed in the sinuses. A highly pulsatile jet is propelled from the left ventricle during systole and is divided into different portions passing either through the aorta or the SV. The small vortices formed at the tips of the cusps ensure a continuous recirculation of blood in the sinuses during systole. Being dictated by the flow reversal at late systole, the downstream vortices issuing from the top of the leaflets become stronger and allow to push the open cusps toward a quick closure [8], see Fig. 16. The vortices observed in the sinuses play subsequently an essential role to prevent stagnation areas in the sinuses during diastole. The structure of the vortices is drastically modified after TAVI. During the opening phase, the diseased leaflets behave as an obstruction preventing the fluid to be correctly pushed in the sinuses. The only zones allowing fluid penetration in the sinuses are situated around the tips of the cusps. The bigger the surface of the calcified cusps is, the more difficult the fluid penetration becomes. Accordingly, the presence of the diseased cusps prevents the complete fluid recirculation and reduces  $\dot{\gamma}$  in the sinuses.

We have performed a systematic analysis on the occurrence of stagnation zones with respect to the area of the calcified leaflets. The computational results reported in Fig. 22 show that, by increasing A (L in 2D), dead zones with low shear rates below  $5 \text{ s}^{-1}$  are created above a threshold value. An increased thromboembolic risk is subsequently expected as the size of the calcification increases. Therefore, it seems mandatory to eliminate the localized stagnant zones which are inaccessible to blood after TAVI. However, it is interesting to note that, at a fixed calcified leaflet area, the low shear stress at dead zones increases gradually if the prescribed cardiac output, referred to as CO, increases, see Fig. 22 (right). Our hypothesis is as follows. Under an increased blood volume ejected by the left ventricle, due for example to exercise or in response to certain classes of drugs, blood supply to the sinuses increases and leads to the reduction of stagnation zones.

## 5. Concluding remarks

This article concerns the numerical modeling of the fluid dynamics in full aorta in the presence of the aortic. To this aim, we have improved the RIS methodology developed in Laadhari et al. [28]. In summary, the main contributions of this work reside in that: (i) The simulations are performed in the full aorta allowing the three-dimensional description of the flow near the valve at affordable cost compared to the full FSI models; (ii) The coupling between the flow and valve dynamics relies on a Lagrange multiplier rather than a penalty term, for which the tuning is often problematic and may induce instabilities

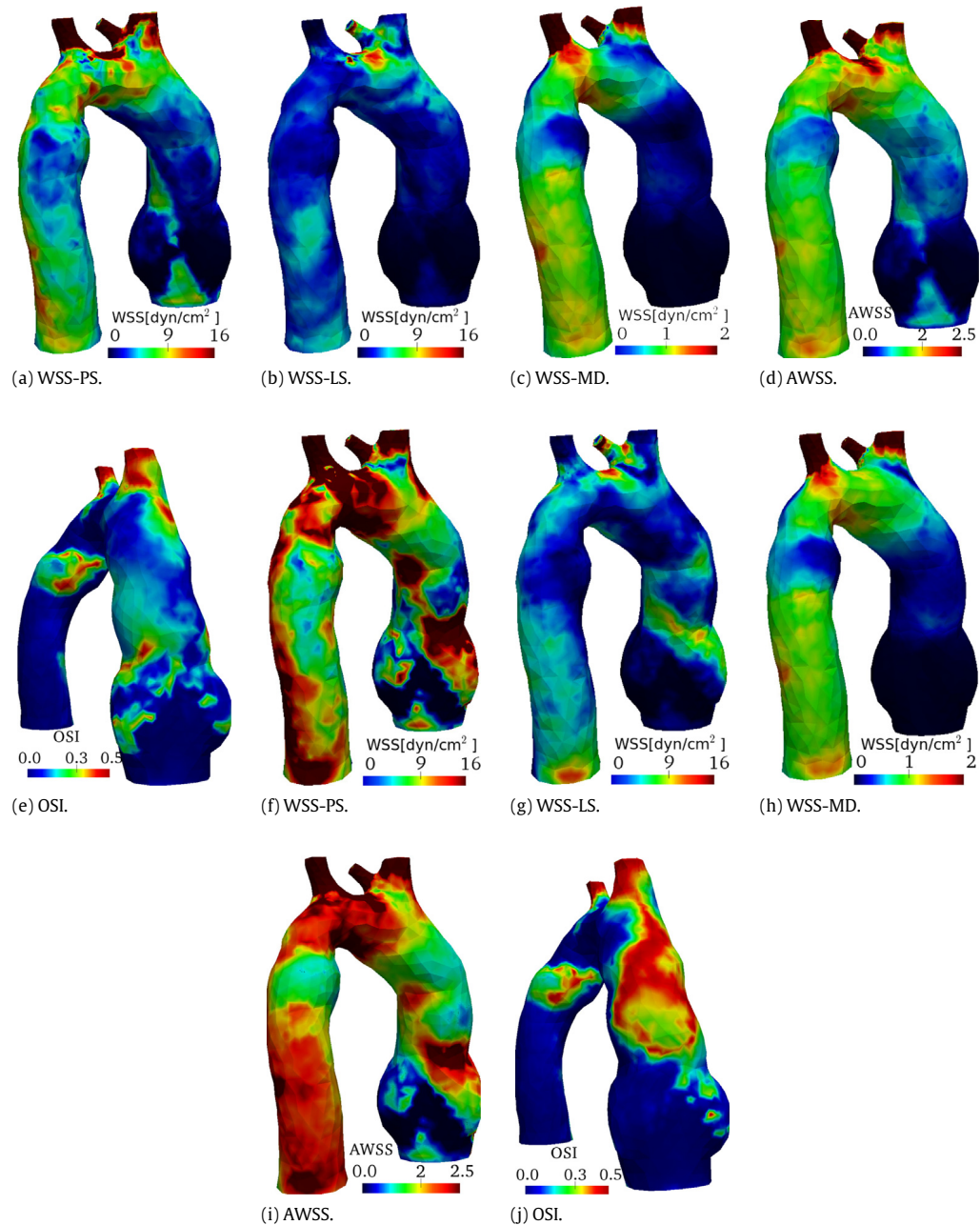


**Fig. 20.** Example 4. Snapshots showing the WSS, AWSS and OSI in the cases of healthy (top row) and stenotic (bottom row) aortic valves.

especially when flow and geometry become complex; (iii) A banded level set variant helps to assemble the surface integral terms only in a surrounding domain of the valve, allowing thereby to address the singularity of the linear system and featuring comparable computational cost with respect to the RIS method; (iv) Different numerical strategies are proposed, and the solution method is based on the numerical investigation of the different algorithmic choices. That guarantees sufficient stability when the geometry and flow become complex; (v) Numerical examples in 2D and 3D for healthy and pathological valves allow to address in detail the relevance of the mathematical model in terms of physiological meaning. Comparisons with clinical measurements and numerical results in a patient-specific case show good agreement; and (vi) The flexibility of the model allows to study the hemodynamics in the SV after TAVI, showing that blood may be subject to stagnation in the sinuses and resulting in potential thromboembolic complications. Although we considered idealized shapes for the heavily calcified leaflets, this study can serve as a starting point to better understand the stagnation extent in patient-specific cases. Systematic clinical studies would be necessary to accept or reject the present concern. If confirmed,

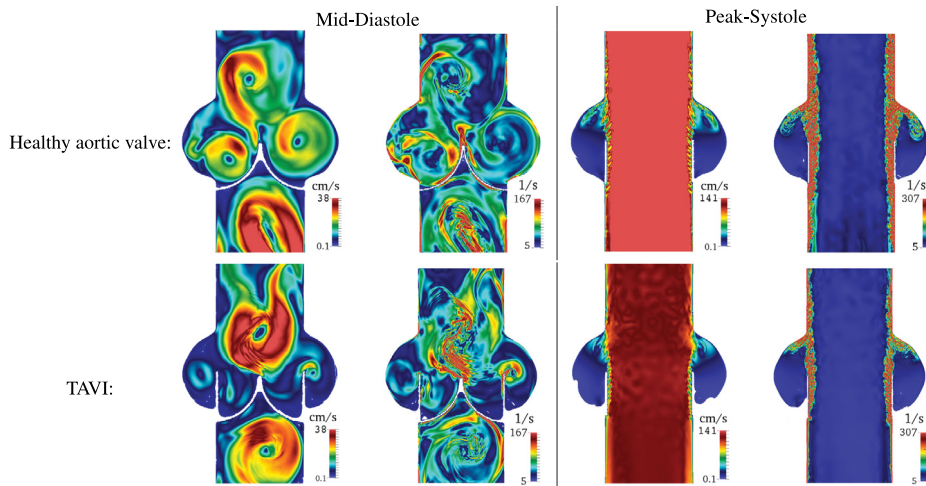


**Fig. 21.** Example 5. Flow features and stagnation areas. Velocity magnitude and shear rate in MD (left) and PS (right). Top: healthy valve. Bottom: after TAVI. The white color corresponds to  $\mathbf{u} \in [0, 0.1]$  cm/s and  $\dot{\gamma} \in [0, 5]$  s<sup>-1</sup>.

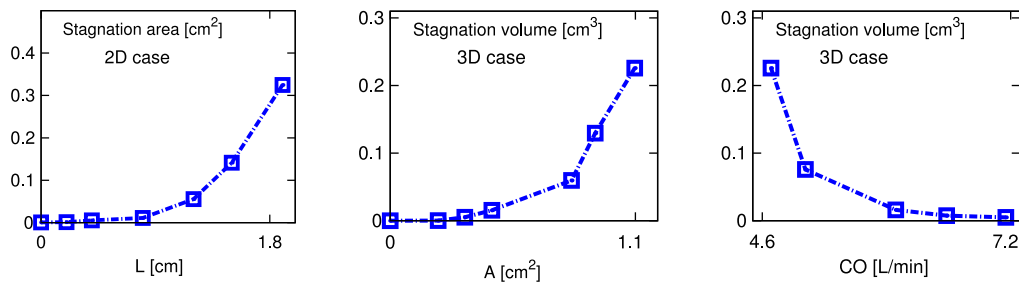


**Fig. 22.** Example 5. Change in the stagnation zone after TAVI with respect to the calcification area and the cardiac output.

this warning can have major implications on the evaluation of interventional outcomes after TAVI. Appropriate anticoagulant medication may be advisable to overcome this thromboembolic risk.

However, several limitations of our model exist, mainly in terms of physiological relevance. We clarify that our primary intention was to introduce a relatively simple framework that could be progressively enriched. In this regard, we list some of the straightforward extensions. We are currently developing a fully Eulerian fluid–membrane interaction method for the simulation of the mechanical properties of extremely thin leaflets. We are also investigating the model for flexible leaflets developed in [57]. In addition, further improvements need to model the aortic wall compliance to account for its effect on the flow pattern mainly near the valve. We also foresee the applicability of the proposed framework to study the hemodynamics after TAVI in more realistic patient-specific cases. Finally, the development of a model including a complete set of valves within the full heart represents our ultimate goal. A huge obstacle towards this aim consists in elaborating suitable approaches to include the papillary muscles and the chordae tendinae.

## Acknowledgments

We gratefully acknowledge the financial support by the Swiss National Science Foundation through the grant 320030-149567. AL would like to thank Prof. Alfio Quarteroni (Mathematics Institute of Computational Science and Engineering, EPFL, Switzerland) for fruitful discussions.

## Appendix A. Supplementary material

Supplementary material related to this article can be found online at <http://dx.doi.org/10.1016/j.cam.2016.11.042>.

## References

- [1] J. de Hart, G.W.M. Peters, P.J.G. Schreurs, F.P.T. Baaijens, A three-dimensional computational analysis of fluid–structure interaction in the aortic valve, *J. Biomech.* 36 (1) (2003) 103–112. <http://dx.doi.org/10.1114/B:ABME.0000049032.51742.10>.

- [2] K. Chandran, Role of computational simulations in heart valve dynamics and design of valvular prostheses, *Cardiovasc. Eng. Technol.* 1 (2010) 18–38. <http://dx.doi.org/10.1007/s13239-010-0002-x>, Springer US.
- [3] B.J. Bellhouse, Velocity and pressure distributions in the aortic valve, *J. Fluid Mech.* 37 (1969) 587. <http://dx.doi.org/10.1017/S0022112069000747>.
- [4] F.K. Wippermann, On the fluid dynamics of the aortic valve, *J. Fluid Mech.* 159 (1985) 487–501. <http://dx.doi.org/10.1017/S0022112085003317>.
- [5] Y. Henderson, N.E. Johnson, Velocity and pressure distributions in the aortic valve, *Heart* 4 (1912) 69. <http://dx.doi.org/10.1017/S0022112069000747>.
- [6] M. Astorino, J. Hamers, S.C. Shadden, J.-F. Gerbeau, A robust and efficient valve model based on resistive immersed surfaces, *Int. J. Numer. Methods Biomed. Eng.* 28 (9) (2012) 937–959. <http://dx.doi.org/10.1002/cnm.2474>.
- [7] E. Jung, W. Lee, Lumped parameter models of cardiovascular circulation in normal and arrhythmia cases, *J. Korean Math. Soc.* 43 (4) (2006) 885–897. <http://dx.doi.org/10.4134/JKMS.2006.43.4.885>.
- [8] T. Korakianitis, Y. Shi, A concentrated parameter model for the human cardiovascular system including heart valve dynamics and atrioventricular interaction, *Med. Eng. Phys.* 28 (7) (2006) 613–628. <http://dx.doi.org/10.1016/j.medengphy.2005.10.004>.
- [9] Y. Shi, P. Lawford, R. Hose, Review of zero-D and 1-D models of blood flow in the cardiovascular system, *Biomed. Eng. Online* 10 (2011) 33. <http://dx.doi.org/10.1186/1475-925X-10-33>.
- [10] F. Migliavacca, R. Balossino, G. Pennati, G. Dubini, T.Y. Hsia, M.R. de Leval, E.L. Bove, Multiscale modelling in biofluidynamics: Application to reconstructive paediatric cardiac surgery, *J. Biomech.* 39 (2006) 1010–1020. <http://dx.doi.org/10.1016/j.jbiomech.2005.02.021>.
- [11] F.Y. Liang, S. Takagi, R. Himeno, H. Liu, Biomechanical characterization of ventricular-arterial coupling during ageing: A multi-scale model study, *J. Biomech.* 42 (2009) 692–704. <http://dx.doi.org/10.1016/j.jbiomech.2009.01.010>.
- [12] W. Kroon, W. Huberts, M. Bosboom, F. van de Vosse, A numerical method of reduced complexity for simulating vascular hemodynamics using coupled 0D lumped and 1D wave propagation models, *Comput. Math. Methods Med.* (2012) 156094. <http://dx.doi.org/10.1109/IEMBS.2010.5626619>.
- [13] C.S. Peskin, Flow patterns around heart valves: a numerical method, *J. Comput. Phys.* 10 (1972) 252–271. [http://dx.doi.org/10.1016/0021-9991\(72\)90065-4](http://dx.doi.org/10.1016/0021-9991(72)90065-4).
- [14] M.S. Olufsen, Structured tree outflow condition for blood flow in larger systemic arteries, *Am. J. Physiol.* 276 (1999) H257–H268. <http://dx.doi.org/10.1151/1.1326031>.
- [15] F.N. Van De Vosse, Mathematical modelling of the cardiovascular system, *J. Engrg. Math.* 47 (2003) 175–183. <http://dx.doi.org/10.1023/B:ENGI.0000007986.69547.5a>.
- [16] R. Cheng, Y.G. Lai, K.B. Chandran, Three-dimensional fluid–structure interaction simulation of bileaflet mechanical heart valve flow dynamics, *Ann. Biomed. Eng.* 32 (11) (2004) 1471–1483. <http://dx.doi.org/10.1114/B:ABME.0000049032.51742.10>.
- [17] B. Su, L. Zhong, X.-K. Wang, J.-M. Zhang, R.S. Tan, J.C. Allen, S.K. Tan, S. Kim, H.L. Leo, Numerical simulation of patient-specific left ventricular model with both mitral and aortic valves by FSI approach, *Comput. Methods Programs Biomed.* 113 (2) (2014) 474–482. <http://dx.doi.org/10.1016/j.cmpb.2013.11.009>.
- [18] R. van Loon, P.D. Anderson, F.N. van de Vosse, A fluid–structure interaction method with solid–rigid contact for heart valve dynamics, *J. Comput. Phys.* 217 (2006) 806–823. <http://dx.doi.org/10.1016/j.jcp.2006.01.032>.
- [19] S.C. Vigmostad, H.S. Udaykumar, J. Lu, K.B. Chandran, Fluid–structure interaction methods in biological flows with special emphasis on heart valve dynamics, *Int. J. Numer. Methods Biomed. Eng.* 26 (3–4) (2010) 435–470. <http://dx.doi.org/10.1002/cnm.1340>.
- [20] C. Capelli, G.M. Bosi, E. Cerri, J. Nordmeyer, T. Odenwald, P. Bonhoeffer, F. Migliavacca, A.M. Taylor, S. Schievano, Patient-specific simulations of transcatheter aortic valve stent implantation, *Med. Biol. Eng. Comput.* 50 (2) (2012) 183–192. <http://dx.doi.org/10.1007/s11517-012-0864-1>.
- [21] K.S. Kunzelman, D.R. Einstein, R.P. Cochran, Fluid–structure interaction models of the mitral valve: function in normal and pathological states, *Philos. Trans. R. Soc. Lond. B Biol. Sci.* 362 (1484) (2007) 1393–1406. <http://dx.doi.org/10.1098/rstb.2007.2123>.
- [22] D.R. Einstein, F. Del Pin, X. Jiao, A.P. Kuprat, J.P. Carson, K.S. Kunzelman, R.P. Cochran, J.M. Guccione, M.B. Ratcliffe, Fluid–structure interactions of the mitral valve and left heart: Comprehensive strategies, past, present and future, *Internat. J. Numer. Methods Engrg.* 26 (3–4) (2010) 348–380. <http://dx.doi.org/10.1002/cnm.1280>.
- [23] I. Borazjani, Fluid–structure interaction, immersed boundary–finite element method simulations of bio-prosthetic heart valves, *Comput. Methods Appl. Mech. Engrg.* 257 (2013) 103–116. <http://dx.doi.org/10.1016/j.cma.2013.01.010>.
- [24] T. Bao, L. F. Sotiropoulos, Fluid–structure interaction of an aortic heart valve prosthesis driven by an animated anatomic left ventricle, *J. Comput. Phys.* 244 (1) (2013) 41–62. <http://dx.doi.org/10.1016/j.jcp.2012.08.036>.
- [25] H. Gao, X. Ma, N. Qi, C. Berry, B.E. Griffith, X. Luo, A finite strain nonlinear human mitral valve model with fluid–structure interaction, *Int. J. Numer. Methods Biomed. Eng.* 30 (2014) 1597–1613. <http://dx.doi.org/10.1002/cnm.2691>.
- [26] B.E. Griffith, *Simulating the blood–muscle–valve mechanics of the heart by an adaptive and parallel version of the immersed boundary method (Ph.D. thesis)*, Courant Institute of Mathematical Sciences, New York University, 2005.
- [27] B.E. Griffith, Immersed boundary model of aortic heart valve dynamics with physiological driving and loading conditions, *Int. J. Numer. Methods Biomed. Eng.* 28 (3) (2011) 317–345. <http://dx.doi.org/10.1002/cnm.1445>.
- [28] A. Laadhari, A. Quarteroni, Numerical modeling of heart valves using resistive Eulerian surfaces, *Int. J. Numer. Methods Biomed. Eng.* 32 (5) (2016) <http://dx.doi.org/10.1002/cnm.2743>.
- [29] J.D. Newton, S. Redwood, B.D. Prendergast, Transcatheter aortic valve implantation: a durable treatment option in aortic stenosis? *Heart* 101 (12) (2015) 913–914. <http://dx.doi.org/10.1136/heartjnl-2014-307332>.
- [30] R.V. Freeman, C.M. Otto, Spectrum of calcific aortic valve disease. Pathogenesis, disease progression and treatment strategies, *Circulation* 111 (2015) 3316–3326. <http://dx.doi.org/10.1161/CIRCULATIONAHA.104.486738>.
- [31] Y.-R. Woo, A.P. Yoganathan, In vitro pulsatile flow velocity and shear stress measurements in the vicinity of mechanical mitral heart prostheses, *J. Biomech.* 19 (1986) 39–51. [http://dx.doi.org/10.1016/0021-9290\(86\)90107-7](http://dx.doi.org/10.1016/0021-9290(86)90107-7).
- [32] K.A. Barbee, Role of subcellular shear-stress distributions in endothelial cell mechanotransduction, *Ann. Biomed. Eng.* 30 (4) (2002) 472–482. <http://dx.doi.org/10.1114/1.1467678>.
- [33] X. Liu, Y. Fan, X. Deng, F. Zhan, Effect of non-newtonian and pulsatile blood flow on mass transport in the human aorta, *J. Biomech.* 44 (6) (2011) 1123–1131. <http://dx.doi.org/10.1016/j.jbiomech.2011.01.024>.
- [34] N. Shahcheraghi, H.A. Dwyer, A.Y. Cheer, A.I. Barakat, R. Rutaganira, Unsteady and three-dimensional simulation of blood flow in the human aortic arch, *J. Biomech. Eng.* 124 (2002) 378. <http://dx.doi.org/10.1115/1.1487357>.
- [35] A.F. Stalder, A. Frydrychowicz, M.F. Russe, J.G. Korvink, J. Hennig, K. Li, M. Markl, Assessment of flow instabilities in the healthy aorta using flow-sensitive MRI, *J. Magn. Reson. Imaging* 33 (4) (2011) 839–846. <http://dx.doi.org/10.1002/jmri.22512>.
- [36] H.N. Sabbah, P.D. Stein, Turbulent blood flow in humans: its primary role in the production of ejection murmurs, *Circ. Res.* 38 (6) (1976) 513–525. <http://dx.doi.org/10.1161/01.RES.38.6.513>.
- [37] L. Buellesfeld, S. Stortecky, B. Kalesan, S. Gloekler, A.A. Khattab, F. Nietlispach, V. Delfine, C. Huber, B. Eberle, B. Meier, P. Wenaweser, S. Windecker, Aortic root dimensions among patients with severe aortic stenosis undergoing transcatheter aortic valve replacement, *JACC Cardiovasc. Interv.* 6 (1) (2013) 72–83. <http://dx.doi.org/10.1016/j.jcin.2012.09.007>.
- [38] M.R. Labrosse, C.J. Beller, F. Robicsek, M.J. Thubrikar, Geometric modeling of functional trileaflet aortic valves: development and clinical applications, *J. Biomech.* 39 (14) (2006) 2665–2672. <http://dx.doi.org/10.1016/j.jbiomech.2005.08.012>.
- [39] M. Swanson, R.E. Clark, Dimensions and geometric relationships of the human aortic valve as a function of pressure, *Circ. Res.* 35 (6) (1974) 871–882. <http://dx.doi.org/10.1161/01>.
- [40] D. Zhu, Z. Qiang, Dynamic normal aortic root diameters: implications for aortic root reconstruction, *Ann. Thorac. Surg.* 91 (2) (2010) 485–489. <http://dx.doi.org/10.1016/j.athoracsur.2010.10.058>.
- [41] A. Laadhari, P. Saramito, C. Misbah, An adaptive finite element method for the modeling of the equilibrium of red blood cells, *Internat. J. Numer. Methods Fluids* 80 (2016) 397–428. <http://dx.doi.org/10.1002/fld.4086>.

- [42] J. Schöberl, NETGEN An advancing front 2D/3D–mesh generator based on abstract rules, *Comput. Vis. Sci.* 1 (1) (1997) 41–52. <http://dx.doi.org/10.1007/s007910050004>.
- [43] S. Chandra, N.M. Rajamannan, P. Sucusky, Computational assessment of bicuspid aortic valve wall–shear stress: implications for calcific aortic valve disease, *Biomech. Model. Mechanobiol.* 11 (7) (2012) 1085–1096. <http://dx.doi.org/10.1007/s10237-012-0375-x>.
- [44] H. Borouchaki, P.L. George, B. Mohammadi, Delaunay mesh generation governed by metric specifications Part II. Applications, *Finite Elem. Anal. Des.* 25 (1997) 85–109. [http://dx.doi.org/10.1016/S0168-874X\(96\)00065-0](http://dx.doi.org/10.1016/S0168-874X(96)00065-0).
- [45] F. Hecht, Bidimensional Anisotropic Mesh Generator, 2006. [www.people.sc.fsu.edu/~jburkardt/data/bamg/bamg](http://www.people.sc.fsu.edu/~jburkardt/data/bamg/bamg) (Accessed: 26.09.16).
- [46] F. Brezzi, M. Fortin, Mixed and Hybrid Finite Element Methods, Vol. 15, Springer, New York, 1991, <http://dx.doi.org/10.1007/978-1-4612-3172-1>.
- [47] A. Quarteroni, R. Sacco, F. Saleri, Numerical Mathematics, Vol. 37, Springer-Verlag, New York, 2000, <http://dx.doi.org/10.1007/b98885>.
- [48] J.E. Dennis, R.B. Schnabel, Numerical Methods for Unconstrained Optimization and Nonlinear Equations, Prentice-Hall, Englewood Cliffs, NJ, 1983, <http://dx.doi.org/10.1137/1028131>.
- [49] D.F. Griffiths, D.J. Higham, Numerical methods for ordinary differential equations, in: Initial Value Problems, Springer, London, 2010, <http://dx.doi.org/10.1007/978-0-85729-148-6>.
- [50] P. Saramito, Efficient C++ finite element computing with Rheolef, CNRS-CCSD ed., 2013. <http://www-ljk.imag.fr/membres/Pierre.Saramito/rheolef/rheolef-refman.pdf> (Accessed: 22.09.16).
- [51] S. Cito, J. Pallarés, A. Vernet, Sensitivity analysis of the boundary conditions in simulations of the flow in an aortic coarctation at rest and stress conditions, in: Statistical Atlases and Computational Models of the Heart. Imaging and Modelling Challenges: 4th International Workshop, STACOM 2013, Springer, Berlin, Heidelberg, 2014, [http://dx.doi.org/10.1007/978-3-642-54268-8\\_9](http://dx.doi.org/10.1007/978-3-642-54268-8_9).
- [52] J. Schaller, L. Goubergrits, P. Yevtushenko, U. Kertzscher, E. Riesenkampff, T. Kuehne, Hemodynamic in aortic coarctation using mri-based inflow condition, in: Statistical Atlases and Computational Models of the Heart. Imaging and Modelling Challenges: 4th International Workshop, STACOM 2013, 2013, 2014, pp. 65–73. <http://dx.doi.org/10.1007/s10439-013-0879-2>.
- [53] J. García, P. Pibarot, R. Capoulade, F.L. Ven, L. Kadem, E. Larose, Usefulness of cardiovascular magnetic resonance imaging for the evaluation of valve opening and closing kinetics in aortic stenosis, *Eur. Heart J. Cardiovasc. Imaging* 14 (8) (2013) 819–826. <http://dx.doi.org/10.1093/ehjci/jes314>.
- [54] H. Mohammadi, R. Cartier, R. Mongrain, Review of numerical methods for simulation of the aortic root: Present and future directions, *Int. J. Comput. Methods Eng. Sci. Mech.* 17 (3) (2016) 182–195. <http://dx.doi.org/10.1080/15502287.2016.1189463>.
- [55] H.J. Weiss, V.T. Turitto, H.R. Baumgartner, Role of shear rate and platelets in promoting fibrin formation on rabbit subendothelium - studies utilizing patients with quantitative and qualitative platelet defects, *J. Clin. Invest.* 78 (1986) 1072–1082. <http://dx.doi.org/10.1172/JCI112663>.
- [56] K.S. Sakariassen, S.R. Hanson, Y. Cadroy, Methods and models to evaluate shear-dependent and surface reactivity-dependent antithrombotic efficacy, *Thromb Res.* 104 (2001) 149–174. [http://dx.doi.org/10.1016/S0049-3848\(01\)00344-9](http://dx.doi.org/10.1016/S0049-3848(01)00344-9).
- [57] J. Vierendeels, K. Dumont, P.R. Verdonck, A partitioned strongly coupled fluid–structure interaction method to model heart valve dynamics, *J. Comput. Appl. Math.* 215 (29) (2008) 602–609. <http://dx.doi.org/10.1016/j.cam.2006.04.067>, ACOMEN 2005.